The Astronomical Journal, 166:30 (29pp), 2023 July https://doi.org/10.3847/1538-3881/acdac7

TOI-3984 A b and TOI-5293 A b: Two Temperate Gas Giants Transiting Mid-M Dwarfs in Wide Binary Systems

Caleb I. Cañas[1,2,3,29], Shubham Kanodia[2,3,4], Jessica Libby-Roberts[2,3], Andrea S. J. Lin[2,3], Maria Schutte[5], Luke Powers[2,3], Sinclaire Jones[6,7], Andrew Monson[8], Songhu Wang[9], Guðmundur Stefánsson[7,30], William D. Cochran[10], Paul Robertson[11], Suvrath Mahadevan[2,3,12], Adam F. Kowalski[13,14,15], John Wisniewski[16], Brock A. Parker[17], Alexander Larsen[17], Franklin A. L. Chapman[17], Henry A. Kobulnicky[17], Arvind F. Gupta[2,3], Mark E. Everett[18], Bryan Edward Penprase[19], Gregory Zeimann[20], Corey Beard[11], Chad F. Bender[8], Knicole D. Colón[1], Scott A. Diddams[21,22,23], Connor Fredrick[22,23], Samuel Halverson[24], Joe P. Ninan[25], Lawrence W. Ramsey[2,3], Arpita Roy[26,27], and Christian Schwab[28]

[1] NASA Goddard Space Flight Center, 8800 Greenbelt Road, Greenbelt, MD 20771, USA; c.canas@nasa.gov
[2] Department of Astronomy & Astrophysics, The Pennsylvania State University, 525 Davey Laboratory, University Park, PA 16802, USA
[3] Center for Exoplanets and Habitable Worlds, The Pennsylvania State University, 525 Davey Laboratory, University Park, PA 16802, USA
[4] Earth and Planets Laboratory, Carnegie Institution for Science, 5241 Broad Branch Road NW, Washington, DC 20015, USA
[5] Homer L. Dodge Department of Physics and Astronomy, University of Oklahoma, 440 West Brooks Street, Norman, OK 73019, USA
[6] Department of Astronomy, The Ohio State University, 4055 McPherson Laboratory, Columbus, OH 43210, USA
[7] Department of Astrophysical Sciences, Princeton University, 4 Ivy Lane, Princeton, NJ 08540, USA
[8] Steward Observatory, The University of Arizona, 933 North Cherry Avenue, Tucson, AZ 85721, USA
[9] Department of Astronomy, Indiana University, 727 East 3rd Street, Bloomington, IN 47405-7105, USA
[10] McDonald Observatory and Center for Planetary Systems Habitability, The University of Texas at Austin, Austin, TX 78730, USA
[11] Department of Physics & Astronomy, The University of California, Irvine, Irvine, CA 92697, USA
[12] ETH Zurich, Institute for Particle Physics & Astrophysics, Zurich, Switzerland
[13] National Solar Observatory, University of Colorado Boulder, 3665 Discovery Drive, Boulder, CO 80303, USA
[14] Department of Astrophysical and Planetary Sciences, University of Colorado, 2000 Colorado Avenue, Boulder, CO 80305, USA
[15] Laboratory for Atmospheric and Space Physics, University of Colorado Boulder, 3665 Discovery Drive, Boulder, CO 80303, USA
[16] Department of Physics and Astronomy, George Mason University, Fairfax, VA 22030, USA
[17] Department of Physics & Astronomy, University of Wyoming, Laramie, WY 82070, USA
[18] NSF's National Optical-Infrared Astronomy Research Laboratory, 950 North Cherry Avenue, Tucson, AZ 85719, USA
[19] Soka University of America, Aliso Viejo, CA 92656, USA
[20] Hobby Eberly Telescope, University of Texas at Austin, Austin, TX 78712, USA
[21] Electrical, Computer & Energy Engineering, 425 UCB, University of Colorado, Boulder, CO 80309, USA
[22] Department of Physics, 390 UCB, University of Colorado, Boulder, CO 80309, USA
[23] National Institute of Standards & Technology, 325 Broadway, Boulder, CO 80305, USA
[24] Jet Propulsion Laboratory, California Institute of Technology, 4800 Oak Grove Drive, Pasadena, CA 91109, USA
[25] Department of Astronomy and Astrophysics, Tata Institute of Fundamental Research, Homi Bhabha Road, Colaba, Mumbai 400005, India
[26] Space Telescope Science Institute, 3700 San Martin Drive, Baltimore, MD 21218, USA
[27] Department of Physics and Astronomy, Johns Hopkins University, 3400 North Charles Street, Baltimore, MD 21218, USA
[28] School of Mathematical and Physical Sciences, Macquarie University, Balaclava Road, North Ryde, NSW 2109, Australia
Received 2023 February 14; revised 2023 May 19; accepted 2023 May 30; published 2023 June 27

Abstract

We confirm the planetary nature of two gas giants discovered by TESS to transit M dwarfs with stellar companions at wide separations. TOI-3984 A ($J = 11.93$) is an M4 dwarf hosting a short-period (4.353326 ± 0.000005 days) gas giant ($M_p = 0.14 \pm 0.03\,M_J$ and $R_p = 0.71 \pm 0.02\,R_J$) with a wide-separation white dwarf companion. TOI-5293 A ($J = 12.47$) is an M3 dwarf hosting a short-period (2.930289 ± 0.000004 days) gas giant ($M_p = 0.54 \pm 0.07\,M_J$ and $R_p = 1.06 \pm 0.04\,R_J$) with a wide-separation M dwarf companion. We characterize both systems using a combination of ground- and space-based photometry, speckle imaging, and high-precision radial velocities from the Habitable-zone Planet Finder and NEID spectrographs. TOI-3984 A b ($T_{eq} = 563 \pm 15$ K and TSM $= 138^{+29}_{-27}$) and TOI-5293 A b ($T_{eq} = 675^{+42}_{-30}$ K and TSM $= 92 \pm 14$) are two of the coolest gas giants among the population of hot Jupiter–sized gas planets orbiting M dwarfs and are favorable targets for atmospheric characterization of temperate gas giants and 3D obliquity measurements to probe system architecture and migration scenarios.

Unified Astronomy Thesaurus concepts: Exoplanet systems (484); Extrasolar gaseous giant planets (509)

1. Introduction

Hot Jupiters (defined as $P < 10$ days and $R_p \gtrsim 8\,R_\oplus$ in this work) are a rare class of exoplanets with an occurrence rate of $\lesssim$1% (see Beleznay & Kunimoto 2022, and references therein) around Sun-like stars measured through radial velocity (RV; e.g., Cumming et al. 2008; Mayor et al. 2011; Wright et al. 2012) and photometric (e.g., Howard et al. 2012; Petigura et al. 2018; Zhou et al. 2019) surveys. While the exact formation process is

[29] NASA Postdoctoral Fellow.
[30] NASA Sagan Fellow.

unknown (see the review by Dawson & Johnson 2018), the most promising channels for origins are in situ (e.g., Batygin et al. 2016; Boley et al. 2016) or ex situ formation with gas disk migration (e.g., Lin et al. 1996) or high-eccentricity tidal migration (e.g., Rasio & Ford 1996; Weidenschilling & Marzari 1996; Ford & Rasio 2008; Petrovich 2015a).

Less is known about the formation of hot Jupiters orbiting M dwarfs, which should be difficult to form under the process of core accretion (e.g., Laughlin et al. 2004; Ida & Lin 2005; Kennedy & Kenyon 2008). Surveys of M dwarfs have revealed that (i) small ($R_p < 4\,R_\oplus$) planets on short-period orbits ($P < 200$ days) are more common around M dwarfs than Sun-like stars (e.g., Dressing & Charbonneau 2015; Mulders et al. 2015; Hardegree-Ullman et al. 2019; Hsu et al. 2020) and (ii) low-mass planets ($1\,M_\oplus < M_p < 10\,M_\oplus$) are more frequently found orbiting later-type M dwarfs on short-period orbits ($P < 200$ days; e.g., Bonfils et al. 2013; Tuomi et al. 2014, 2019; Sabotta et al. 2021; Pinamonti et al. 2022). The majority of the aforementioned surveys have not detected any appreciable number of hot Jupiters and can only place upper limits of ∼2% on the intrinsic occurrence rate.

A tighter constraint on the occurrence of hot Jupiters orbiting M dwarfs has been made possible through an analysis of M dwarfs observed in the primary TESS mission (Ricker et al. 2015). Gan et al. (2023) reported an occurrence rate of $0.27\% \pm 0.09\%$ for hot Jupiters orbiting early M dwarfs from an analysis of 60,819 M dwarfs with $10.5 < T < 13.5$ spanning $0.45\,M_\odot < M_\star < 0.65\,M_\odot$. Bryant et al. (2023) independently derived an occurrence rate of $0.194\% \pm 0.072\%$ from an analysis of 91,306 M dwarfs spanning $0.088\,M_\odot < M_\star < 0.71\,M_\odot$. At present, these values are smaller than the occurrence rates for hot Jupiters orbiting Sun-like stars, although they are consistent within 1σ–3σ. An analysis of a larger sample of TESS M dwarfs is needed to refine the occurrence rate and determine whether the M dwarf gas giant population is consistent with the population orbiting Sun-like stars.

In this paper, we confirm the planetary nature of two gas giants transiting the M dwarfs TOI-3984 A ($J = 11.93$, $T = 13.46$) and TOI-5293 A ($J = 12.47$, $T = 13.98$). We characterize these systems using space- and ground-based photometry, speckle imaging, and precision RVs obtained with the Habitable-zone Planet Finder (HPF; Mahadevan et al. 2012, 2014) and NEID (Halverson et al. 2016; Schwab et al. 2016) spectrographs. We derive stellar parameters for the host stars with HPF spectra and jointly model the photometry and RVs to confirm the planetary nature of TOI-3984 A b and TOI-5293 A b.

This paper is structured as follows. Section 2 presents the photometric, imaging, and spectroscopic observations. The best estimates of the stellar parameters and properties are presented in Section 3. The modeling and analysis of the photometry and RVs are presented in Section 4. Section 5 provides further discussion of the nature of these planets and the feasibility of future study. A summary of our key results is presented in Section 6.

2. Observations

2.1. TESS

TESS (Ricker et al. 2015) observed (i) TOI-3984 A (TIC 20182780, Gaia DR3 1291955578869575552) in long-cadence mode (30 minute cadence) during Sectors 23–24 (2020 March 18–2020 May 13) and in short-cadence mode (2 minute cadence) during Sectors 50–51 (2022 April 22–2022 May 18) and (ii) TOI-5293 A (TIC 250111245, Gaia DR3 2640121486388076032) in long-cadence mode during Sector 42 (2021 August 20–2021 September 16). Each star has one planet candidate, TOI-3984.01 and TOI-5293.01, that was identified by the "quick-look pipeline" (QLP[31]; Huang et al. 2020a, 2020b) as part of a search for planet candidates orbiting stars with a TESS magnitude of $T > 12$ (Kunimoto et al. 2022).

We extract the long-cadence photometry from the TESS full-frame images using `eleanor` (Feinstein et al. 2019) to process a cutout of 31×31 pixels from the calibrated full-frame images centered on each target. The light curves from `eleanor`[32] use an aperture that minimizes the hour-binned combined differential photometric precision (see Jenkins et al. 2010) to ensure that sharp features on timescales of a few hours, such as transits, are preserved. Figures 1 and 2 present the apertures used to extract the TESS light curves for TOI-3984 A and TOI-5293 A, respectively. In each figure, panel (a) presents the apertures used to derive the light curve from the latest TESS sector. In panel (b), the region contained in an 11×11 pixel subgrid and the photometric apertures from all TESS sectors are overlaid on images from the Zwicky Transient Facility (ZTF; Bellm et al. 2019; Graham et al. 2019; Masci et al. 2019).

TOI-5293 A has a nearby companion in the optimal aperture (TIC 2052711961, $T = 18.44$, $\Delta G_{\rm RP} = 2.6$) at a separation of $3\farcs57$. The second release of the Pan-STARRS survey (PS1; Chambers et al. 2016; Magnier et al. 2020) measures a PS1 $i' = 17.15$ for the nearby companion, which is too faint to contribute to any significant dilution in the photometry obtained with TESS or small ground-based telescopes described in Sections 2.2.1, 2.2.4, and 2.2.5.

The long-cadence light curves analyzed in this work are the `CORR_FLUX` values produced by `eleanor`. The combined differential photometric precision is the value minimized by `eleanor` when searching for the best aperture and is 5661 ppm for TOI-3984 A and 7089 ppm for TOI-5293 A. Observations where the background flux exceeds a threshold (`FLUX_BKG` > 2.5 × `CORR_FLUX`) or with nonzero data quality flags (see a detailed description in Table 28 in Tenenbaum & Jenkins 2018) are excluded from further analysis.

The short-cadence photometry of TOI-3984 A is obtained from the presearch data-conditioned simple aperture photometry (PDCSAP; Jenkins et al. 2016) light curves available at the Mikulski Archive for Space Telescopes (MAST).[33] The PDCSAP photometry is corrected for instrumental systematics and dilution from other objects contained within the aperture using algorithms developed for the Kepler mission (see Smith et al. 2012; Stumpe et al. 2012). As with the long-cadence photometry, observations with nonzero data quality flags are excluded from further analysis. We perform no additional outlier rejection beyond the data quality flags and application of a background threshold value for long-cadence data. Figures 3 and 4 display the TESS light curves.

2.2. Ground-based Photometry

We observed six transits of TOI-3984 A and five transits of TOI-5293 A using a combination of five separate ground-based

[31] https://tess.mit.edu/qlp/
[32] https://github.com/afeinstein20/eleanor
[33] https://archive.stsci.edu/prepds/tess-data-alerts/

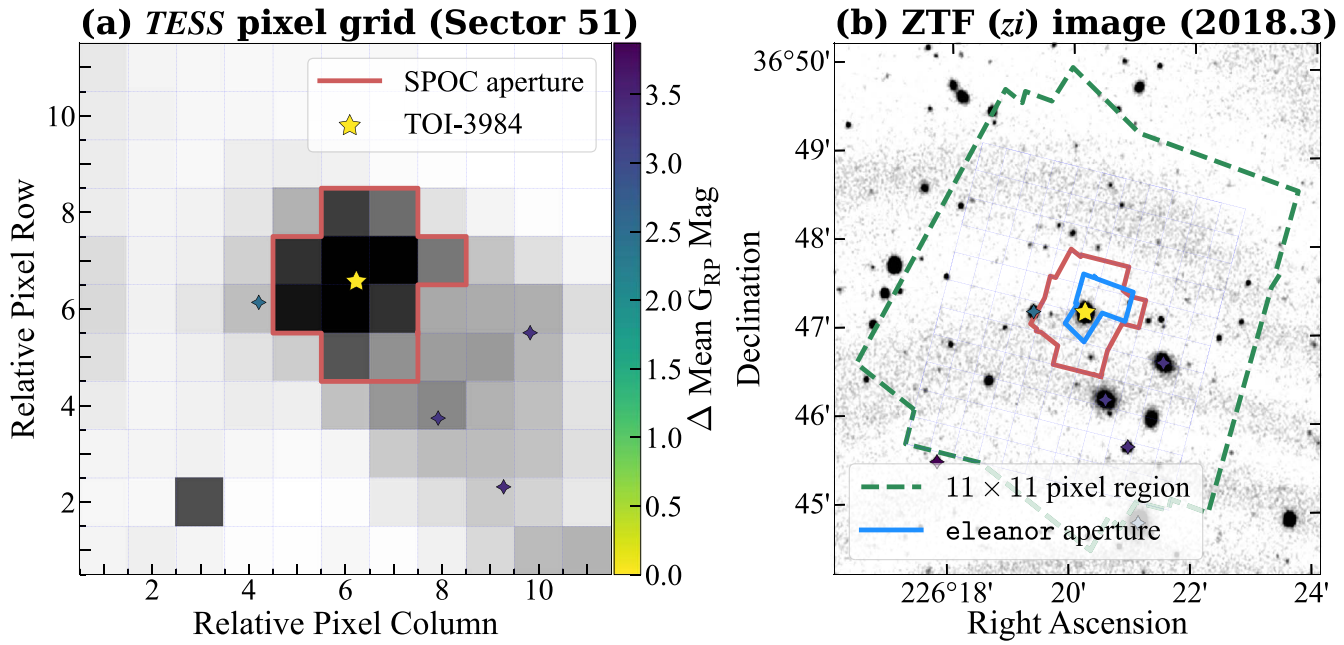

Figure 1. (a) The 11 × 11 TESS target pixel cutout from Sector 51 centered on TOI-3984 A (marked as a star). Stars identified in Gaia DR3 with magnitudes $\Delta G_{RP} < 4$ are marked with diamond stars for reference. (b) Overlay of the region contained in an 11 × 11 pixel grid centered on TOI-3984 A from all sectors (green polygon), the region contained within all SPOC (red polygon) and `eleanor` (blue polygon) photometric apertures, and other comparably bright stars on a ZTF *zi* image.

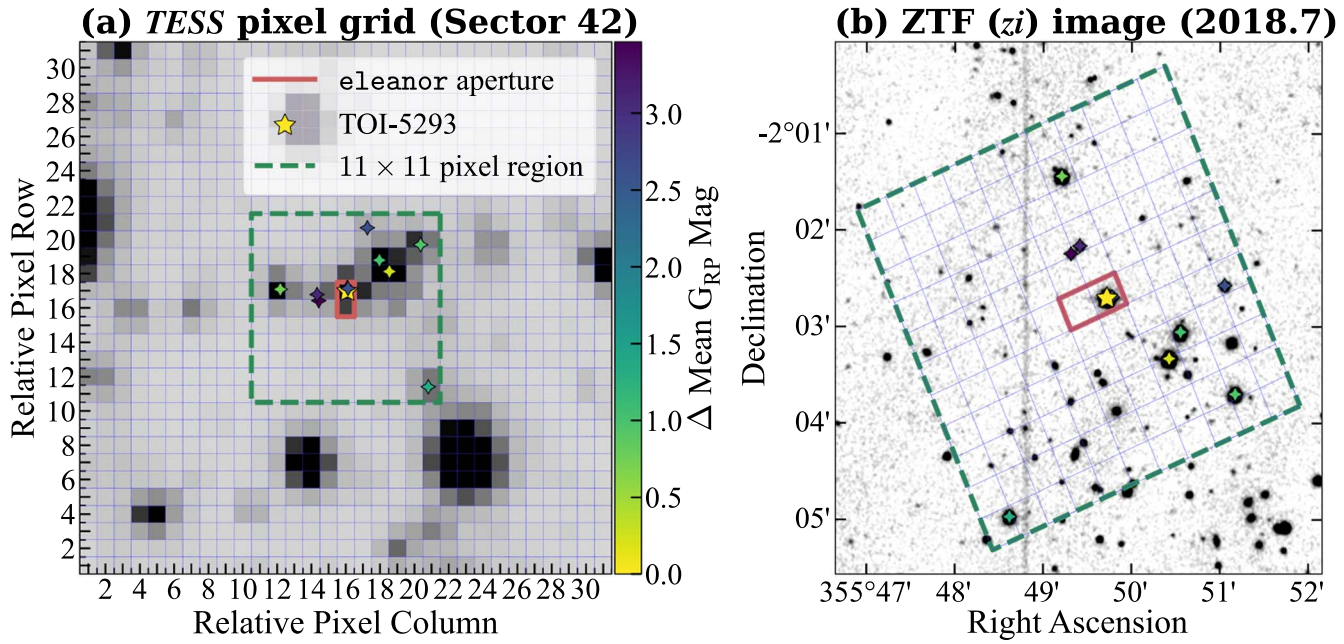

Figure 2. Same as Figure 1 but for TOI-5293 A. (a) The 31 × 31 TESS target pixel cutout centered around TOI-5293 A (marked as a star). Stars identified in Gaia EDR3 having magnitudes $\Delta G_{RP} < 4$ are marked with diamond stars. (b) Overlay of the TESS 11 × 11 pixel subgrid (green polygon), the region contained in the photometric aperture (red polygon), and other comparably bright stars on a ZTF *zi* image.

facilities. All ground-based light curves were derived using `AstroImageJ` (Collins et al. 2017). Following the methodology in Stefánsson et al. (2017), the estimated scintillation noise was included in the flux uncertainty. The light curves are not detrended with any external parameter (e.g., airmass or time). The observations are described in detail below and summarized in Table 1. The ground-based photometry for TOI-5293 A and TOI-3984 A are presented in Figures 4 and 5, respectively.

2.2.1. RBO 0.6 m Telescope

The 0.6 m telescope at the Red Buttes Observatory (RBO) in Wyoming (Kasper et al. 2016) is an f/8.43 Ritchey–Crétien constructed by DFM Engineering, Inc., and equipped with an Apogee Alta F16M camera. We observed (i) TOI-3984 A on the nights of 2021 July 18, 2021 August 13, and 2022 February 3 and (ii) TOI-5293 A on the nights of 2022

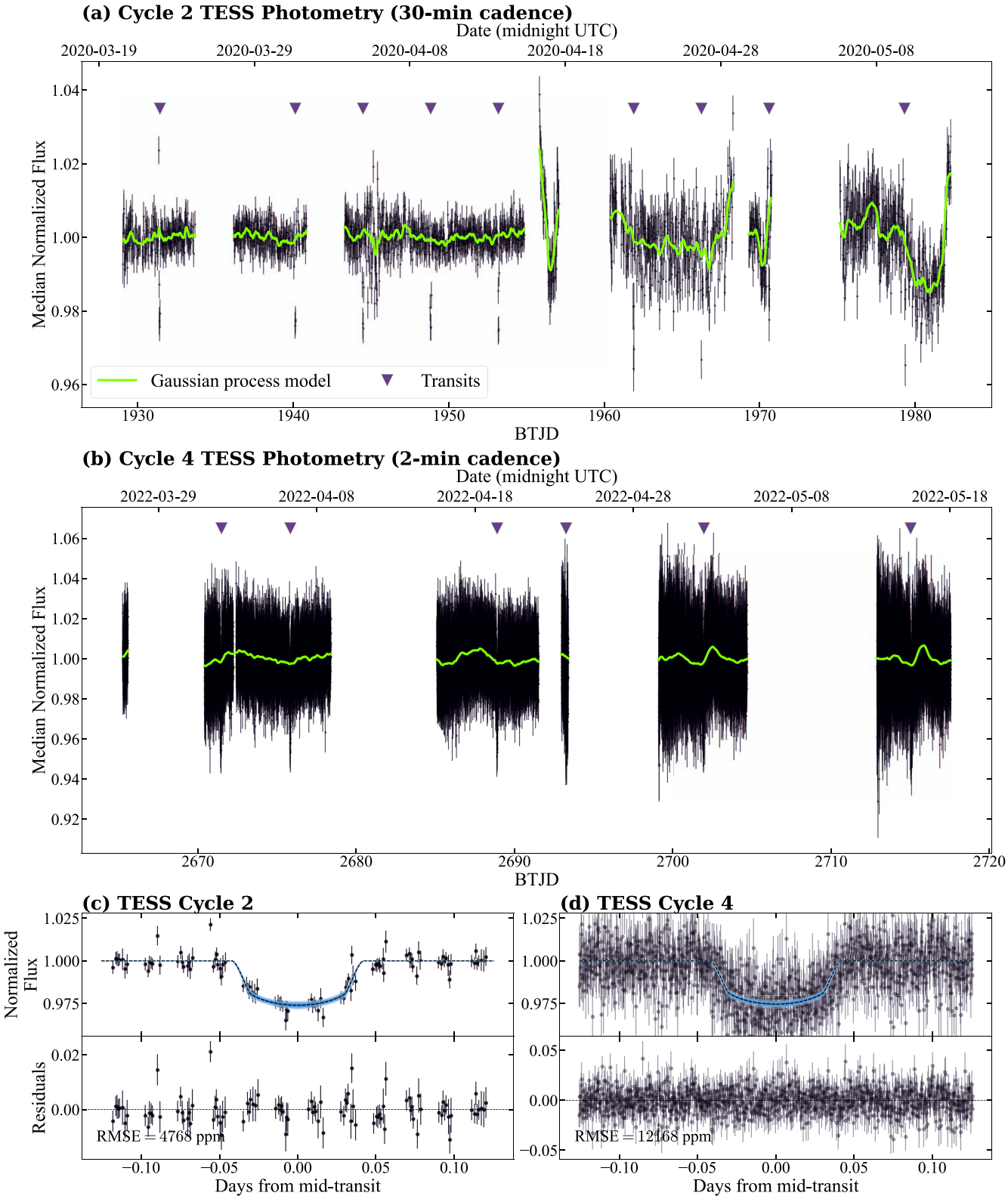

Figure 3. (a) Median normalized TESS long-cadence light curve for TOI-3984 A derived with `eleanor`. The solid green line is the best-fitting Gaussian process model used to detrend the light curve. The triangles indicate the observed transits. (b) Same as panel (a) but for short-cadence TESS data. Panels (c) and (d) show the phase-folded light curves for short- and long-cadence TESS data. In panels (c) and (d), the best-fitting model from the joint fit to the photometry and RVs is plotted as a dashed line, while the shaded regions denote the 1σ (darkest), 2σ, and 3σ (lightest) extent of the model posteriors. The modeling of the photometry and RVs is described in detail in Section 4.

July 27 and 2022 September 12. All observations were moderately defocused, used an exposure time of 240 s, and operated with the Bessell *I* filter (Bessell 1990) and the 2×2 on-chip binning mode, which provides a gain of 1.39 e^{-} ADU^{-1}, a plate scale of $0\farcs731$ $pixel^{-1}$, and a readout time of ∼2.4 s.

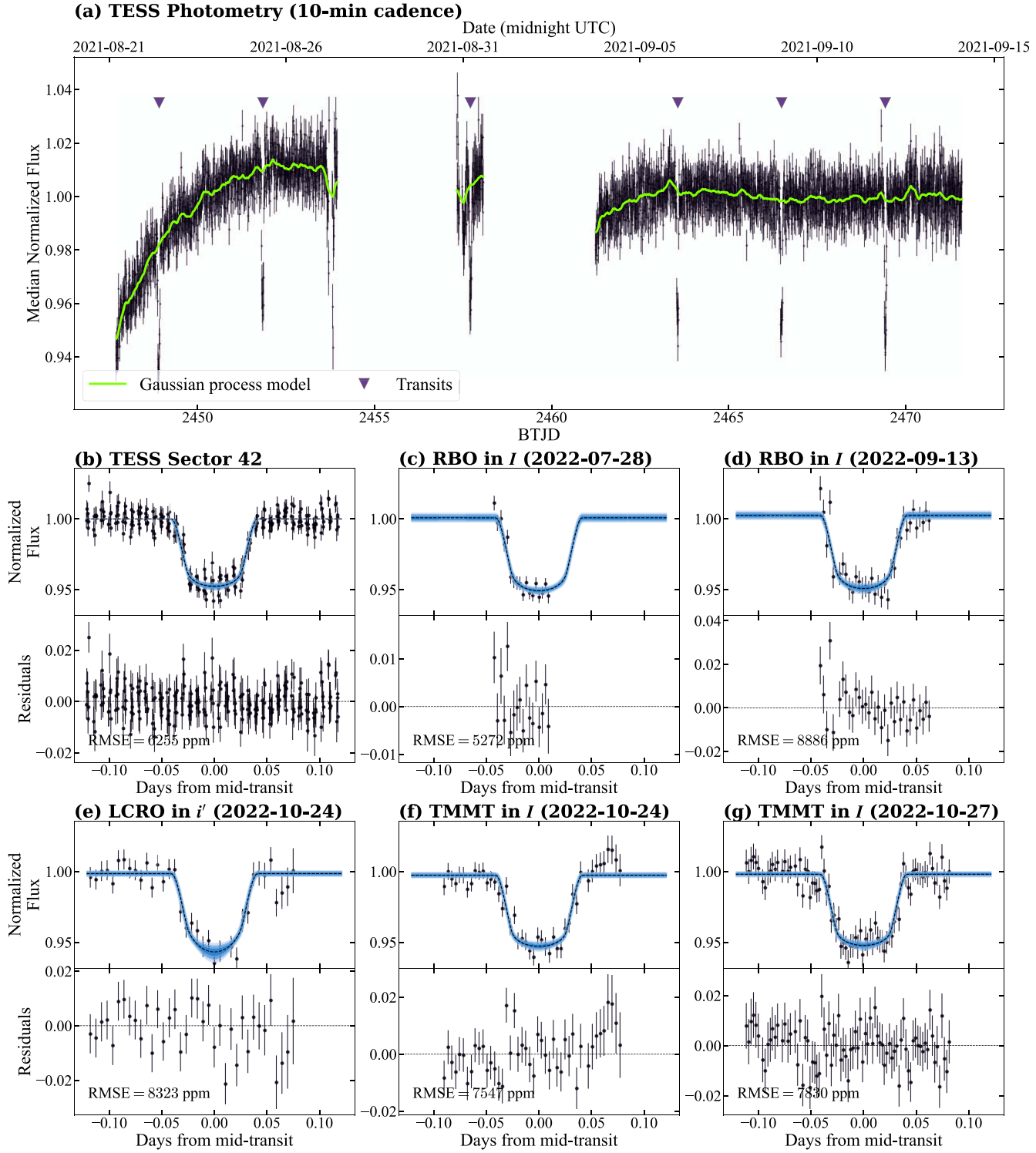

Figure 4. Same as Figure 3 but for TOI-5293 A. (a) Median normalized TESS light curve for TOI-5293 A derived with `eleanor` along with the best-fitting Gaussian process model. The triangles indicate the observed transits. Panels (b)−(g) are the light curves for the TESS, RBO, LCRO, and TMMT plotted with model posteriors (shaded regions) from the joint fit to the photometry and RVs.

2.2.2. SUA Nieves 0.3 m Telescope

The 0.3 m Planewave CDK14 telescope located at the Luis and Linda Nieves Observatory[34] at Soka University of America in Aliso Viejo, California, uses an FLI Proline 16803 camera with a $47' \times 47'$ field of view and a quantum efficiency >50%. We observed TOI-3984 A on the night of 2021 August 13 in the Sloan i' filter using a 300 s exposure time and 1×1 binning mode, which provides a plate scale of $0.''7$ pixel^{-1}.

2.2.3. APO 3.5 m Telescope

We used the 3.5 m Astrophysical Research Consortium (ARC) Telescope Imaging Camera (ARCTIC;

[34] https://sites.soka.edu/SUO/about/

Table 1
Summary of Ground-based Photometry

Civil Night	Facility	Filter	Exposure Time (s)	Aperture and Sky Annulus (pixels and arcsec)
TOI-3984 A				
2021-07-18	RBO	Bessell I	240	10/20/30 (7.3/14.6/21.″9)
2021-08-13	RBO	Bessell I	240	10/20/30 (7.3/14.6/21.″9)
2021-08-13	Soka	Sloan i'	300	10/15/20 (7.0/10.5/14.″0)
2022-02-03	RBO	Bessell I	240	10/20/30 (7.3/14.6/21.″9)
2022-03-23	ARCTIC	Sloan i'	45	20/30/40 (9.1/13.7/18.″2)
2022-05-10	ARCTIC	Sloan z'	30	12/20/30 (5.5/9.1/13.″7)
TOI-5293 A				
2022-07-27	RBO	Bessell I	240	10/20/30 (7.3/14.6/21.″9)
2022-09-12	RBO	Bessell I	240	10/20/30 (7.3/14.6/21.″9)
2022-10-23	LCRO	Sloan i'	420	6/10/15 (4.6/7.7/11.″6)
2022-02-03	TMMT	Bessell I	300	6/10/15 (7.2/11.9/17.″9)
2022-03-23	TMMT	Bessell I	180	6/10/15 (7.2/11.9/17.″9)

Huehnerhoff et al. 2016) on the ARC 3.5 m telescope at Apache Point Observatory (APO) to obtain transits of TOI-3984 A on the nights of 2022 March 23 and 2022 May 10. The observations on 2022 March 23 were performed in the Sloan i' filter using an engineered diffuser (Stefánsson et al. 2017) with an exposure time of 45 s. ARCTIC was operated in the quad amplifier and fast readout modes using the 4×4 on-chip binning mode to achieve a gain of 2 e^- ADU^{-1}, a plate scale of 0.″456 $pixel^{-1}$, and a readout time of 1.3 s. The observation on 2022 May 10 was performed in the Sloan z' filter slightly out of focus with an exposure time of 30 s. Hardware issues prevented the use of quad mode; instead, ARCTIC was operated in the single-amplifier and fast readout modes using the 4×4 on-chip binning mode with a readout time of 11 s.

2.2.4. LCO 0.3 m TMMT Telescope

The robotic Three-hundred MilliMeter Telescope (TMMT; Monson et al. 2017) at Las Campanas Observatory (LCO) is an f/7.8 FRC300 from Takahashi on a German equatorial AP1600 GTO mount with an Apogee Alta U42-D09 CCD camera, FLI ATLAS focuser, and Centerline filter wheel. We observed TOI-5293 A on the nights of 2022 October 23 and 2022 October 26. The observations were performed slightly out of focus in the Bessell I filter (Bessell 1990) with exposure times of 300 and 180 s, respectively, while operating in a 1×1 binning mode. In this mode, TMMT has a gain of 1.35 e^- ADU^{-1}, a plate scale of 1.″194 $pixel^{-1}$, and a readout time of ∼6 s.

2.2.5. LCRO 0.3 m Telescope

The 305 mm Las Campanas Remote Observatory telescope[35] (LCRO) at LCO observed TOI-5293 A on the night of 2022 October 23. The LCRO is an f/8 Maksutov–Cassegrain from Astro-Physics on a German Equatorial AP1600 GTO mount with an FLI Proline 16803 CCD camera, FLI ATLAS focuser, and Centerline filter wheel. The observations were performed slightly out of focus in the Sloan i' filter with an exposure time of 420 s. We used the 1×1 binning mode, providing a gain of 1.52 e^- ADU^{-1}, a plate scale of 0.″773 $pixel^{-1}$, and a readout time of 17 s.

[35] http://lcobot.duckdns.org/

2.3. High-contrast Imaging

NESSI (Scott et al. 2018) is a dual-channel speckle imager on the WIYN 3.5 m telescope at Kitt Peak National Observatory (KPNO). Both TOI-3984 A and TOI-5293 A were observed on 2022 April 18 using NESSI. The faintness of these targets ($r' > 14$) prevented observations in the narrow filters that NESSI traditionally uses, while hardware issues during the observing run only allowed for observing with the redder channel in the Sloan z' filter. The images were reconstructed following the procedures described in Howell et al. (2011).

Figures 6 and 7 display the 5σ contrast curve with insets of the reconstructed NESSI speckle images. The NESSI data reveal no bright ($\Delta z' < 3$) companions and no potential sources of dilution at separations of 0.″2–1.″2 from the host stars. These angular limits correspond to projected spatial limits of 22–130 au for TOI-3984 A and 32–193 au for TOI-5293 A. Adaptive optics imaging of TOI-3984 A (see Gan et al. 2023) obtained with the Palomar High Angular Resolution Observer on the Palomar 5.1 m telescope (Hayward et al. 2001) also reveal that it is an isolated star having a contrast of $\Delta\text{mag} > 6.1$ at distances of >0.″5 (>54 au) from the star in the near-infrared (1–2.5 μm).

2.4. High-precision Spectroscopy

2.4.1. HPF Spectrograph

The HPF (Mahadevan et al. 2012, 2014) is a high-resolution ($R \sim 55{,}000$) fiber-fed (Kanodia et al. 2018), temperature-stabilized (Stefánsson et al. 2016), near-infrared ($\lambda \sim 8080$–12780 Å) spectrograph located on the 10 m Hobby–Eberly Telescope (HET) at McDonald Observatory (Ramsey et al. 1998; Hill et al. 2021). Observations are executed in a queue by the HET resident astronomers (Shetrone et al. 2007). We obtained (i) 35 visits of TOI-3984 A between 2021 August 23 and 2022 May 10 and (ii) 16 visits of TOI-5293 A between 2022 September 10 and 2022 December 1 with median signal-to-noise ratios (S/Ns) per 1D extracted pixel at 1070 nm of 38 and 35, respectively.

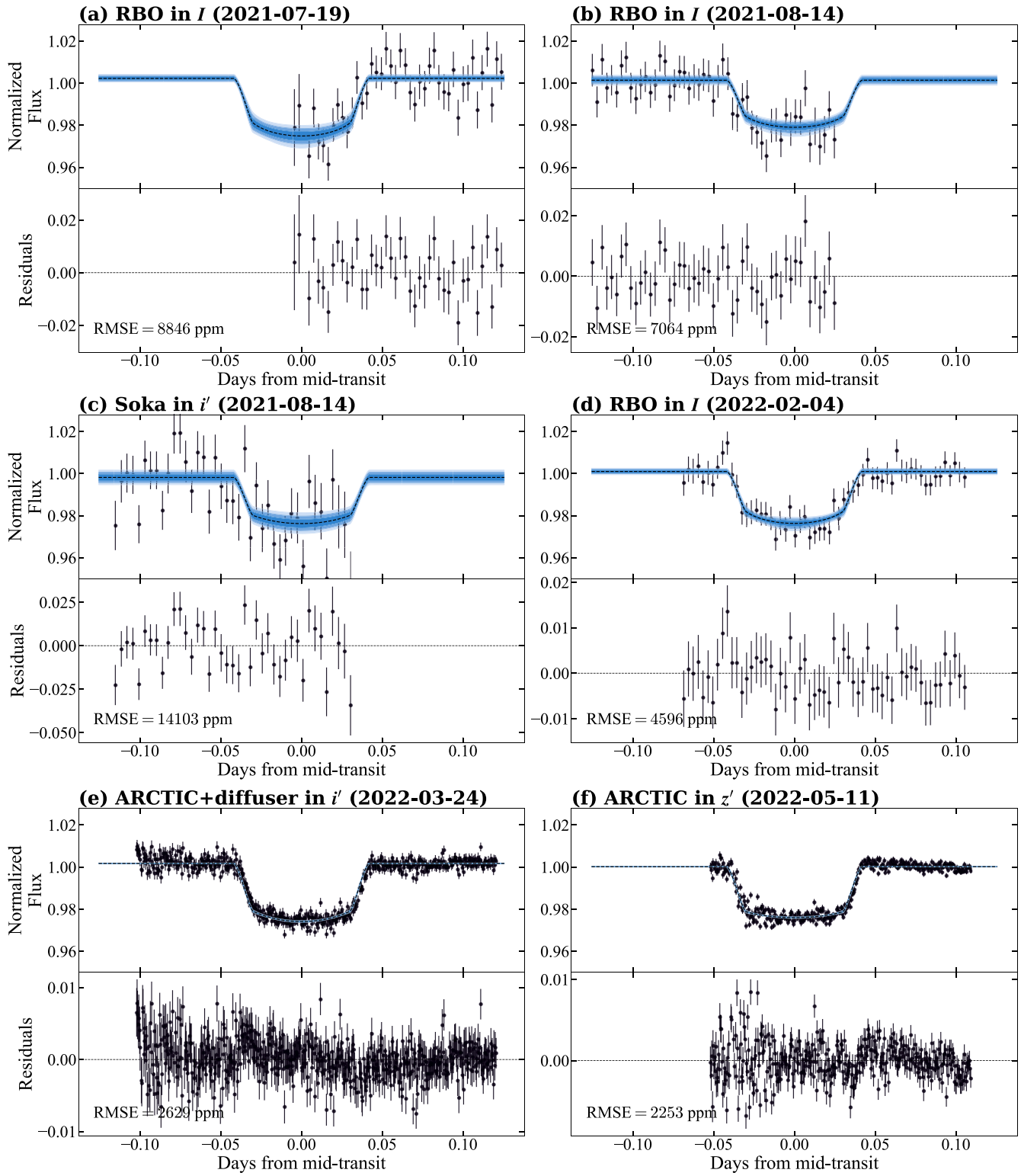

Figure 5. Same as Figure 3 but displaying the ground-based photometry for TOI-3984 A. Panels (a)−(f) are the light curves from RBO, Soka, and ARCTIC plotted with model posteriors (shaded regions) from the joint fit to the photometry and RVs.

The `HxRGproc` tool[36] (Ninan et al. 2018) processed the raw HPF data and performed bias noise removal, nonlinearity correction, cosmic-ray correction, and slope/flux and variance image calculations. The 1D spectra were extracted following the procedures in Ninan et al. (2018), Kaplan et al. (2019), and Metcalf et al. (2019). The wavelength solution and drift correction were extrapolated using laser frequency comb frames obtained from routine calibrations, which enable wavelength calibration on the order of $<30\,\mathrm{cm\,s^{-1}}$ (see Appendix A in Stefánsson et al. 2020a).

The RVs were calculated using a modified version of the `SpEctrum Radial Velocity AnaLyser` code

[36] https://github.com/indiajoe/HxRGproc

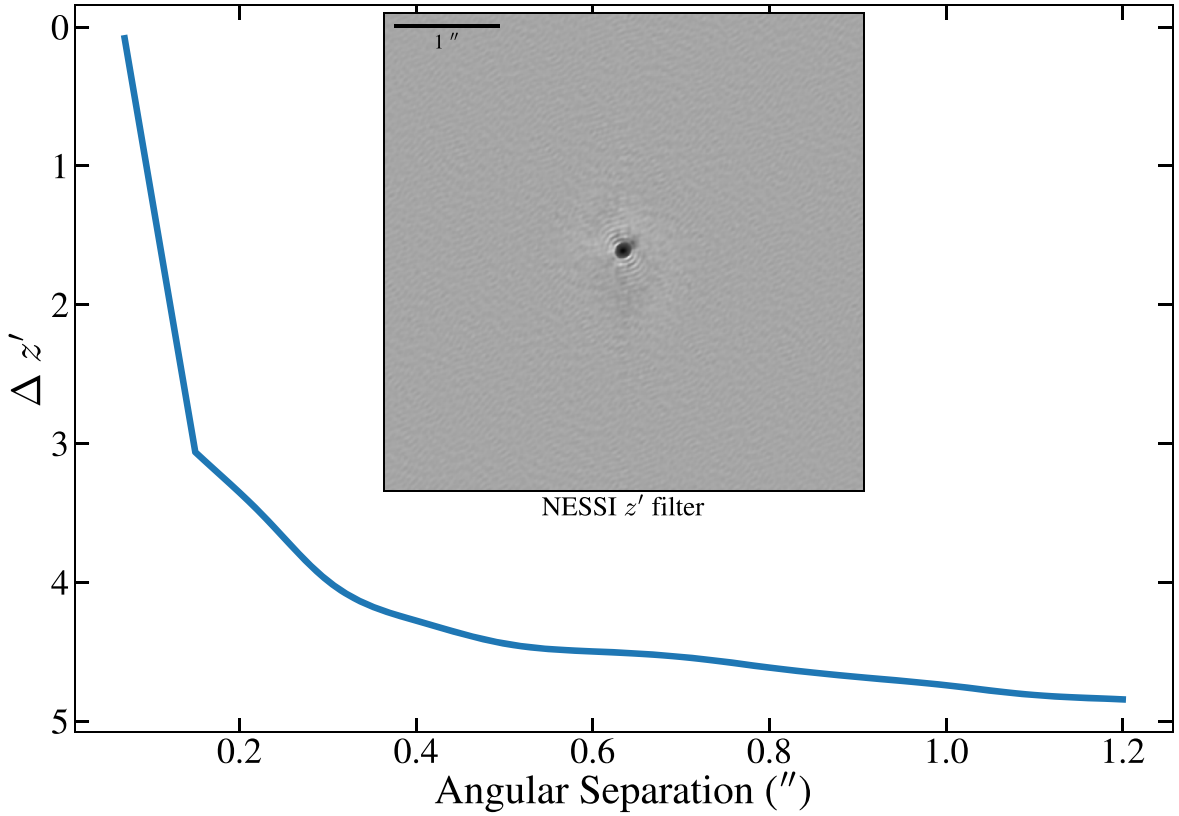

Figure 6. The 5σ contrast curves for TOI-3984 A obtained from speckle imaging with NESSI in the Sloan z' filter. The data reveal no bright companions at separations of $0\overset{''}{.}2$–$1\overset{''}{.}75$. The inset is the $4\overset{''}{.}7 \times 4\overset{''}{.}7$ NESSI speckle image centered on TOI-3984 A in the Sloan z' filter.

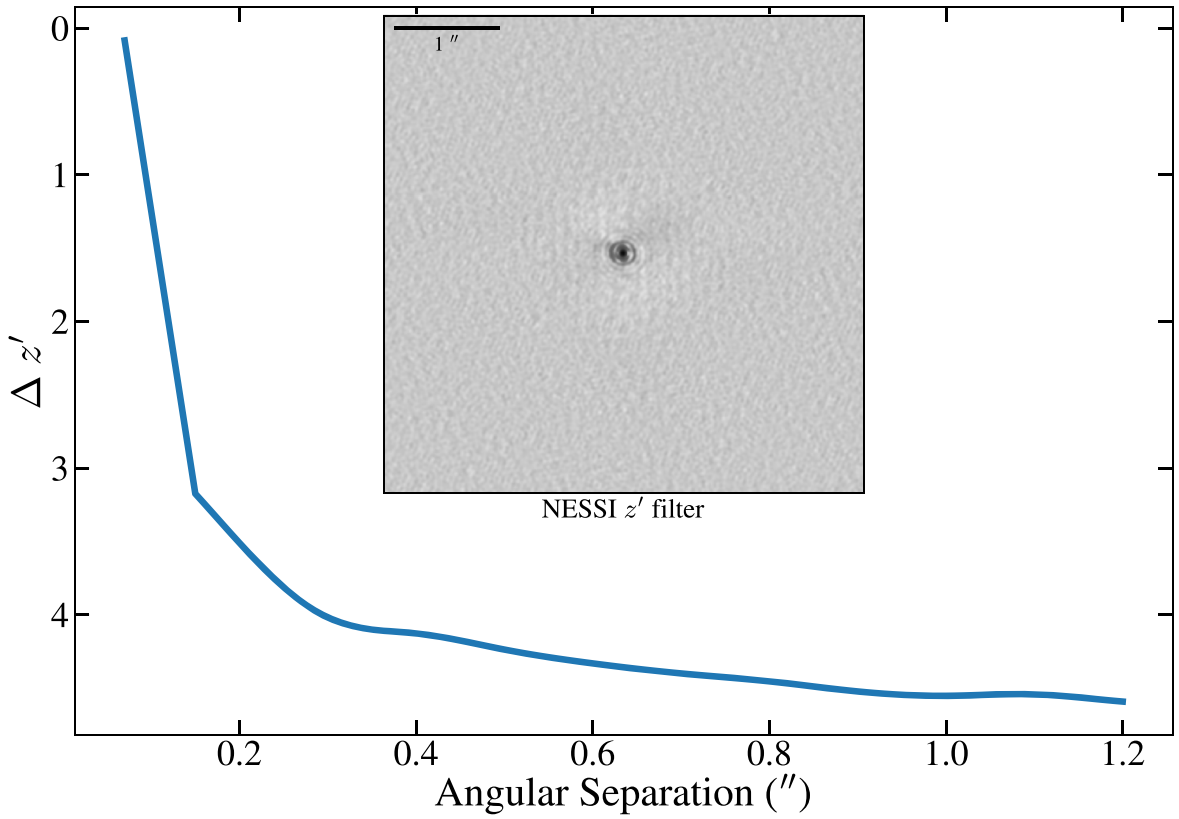

Figure 7. Same as Figure 6 but for TOI-5293 A. Shown is the 5σ contrast curve for TOI-5293 A obtained from speckle imaging using NESSI along with an inset displaying the $4\overset{''}{.}7 \times 4\overset{''}{.}7$ reconstructed speckle image in the Sloan z' filter.

(SERVAL; Zechmeister et al. 2018) optimized for HPF RV extractions (see Metcalf et al. 2019 and Stefánsson et al. 2020a for details). SERVAL uses the template matching technique to derive RVs (e.g., Anglada-Escudé & Butler 2012) and creates a master template from the observations by minimizing the χ^2 statistic. The master template is generated from the observed spectra after masking sky emission lines and telluric regions identified using a synthetic telluric line mask generated from telfit (Gullikson et al. 2014). The barycentric correction is calculated using barycorrpy (Kanodia & Wright 2018). Table 2 reports the HPF RVs, 1σ uncertainties, and S/N per pixel for TOI-3984 A and TOI-5293 A. Figure 8 presents the RVs for TOI-3984 A, and Figure 9 presents the RVs for TOI-5293 A.

2.4.2. NEID Spectrograph

NEID (Halverson et al. 2016; Schwab et al. 2016) is an environmentally stabilized (Stefánsson et al. 2016; Robertson et al. 2019), high-resolution ($R \sim 110{,}000$), fiber-fed (Kanodia et al. 2018) spectrograph with extended red wavelength coverage ($\lambda \sim 3800$–9300 Å) installed on the WIYN 3.5 m telescope at KPNO in Arizona. We obtained six visits of TOI-3984 A between 2022 March 13 and 2022 April 9 in high-resolution mode with a median S/N per 1D extracted pixel of 12 at 850 nm. The NEID data were reduced using the NEID Data Reduction Pipeline,[37] and the level 2 1D extracted spectra were retrieved from the NEID Archive.[38] We measured the RVs using a modified version of the SERVAL code (see Stefánsson et al. 2022) and extracted RVs using the wavelength range from 5440 to 8920 Å (order indices 61–104) and the innermost 3000 pixels of each order (similar to Cañas et al. 2022). Figure 8 presents the RVs, while Table 2 reports the NEID RVs, 1σ uncertainties, and S/N per pixel.

3. Stellar Parameters

3.1. Spectroscopic Parameters

The stellar effective temperature (T_e), surface gravity ($\log g_\star$), and metallicity ([Fe/H]) were calculated using the HPF-SpecMatch[39] package (Stefánsson et al. 2020a), which derives stellar parameters using the empirical template matching methodology discussed in Yee et al. (2017). It uses a two-step χ^2 minimization to identify the five best-matching spectra from a library of well-characterized stars and derives spectroscopic parameters using a weighted linear combination of the library stars. HPF-SpecMatch derives $v \sin i_\star$ by broadening the library spectra using a linear limb-darkening law (Gray 2008). The reported uncertainties are the standard deviation of the residuals from a leave-one-out cross-validation procedure applied to the entire spectral library.

The HPF spectral library contains 166 stars and spans the following parameter space: $2700\ \mathrm{K} < T_e < 6000\ \mathrm{K}$, $4.3 < \log g_\star < 5.3$, and $-0.5 < [\mathrm{Fe/H}] < 0.5$. The library includes 87 M dwarfs ($T_e \leqslant 4000$ K), of which 40 are M dwarfs spanning $3300\ \mathrm{K} \leqslant T_e \leqslant 3700\ \mathrm{K}$, $4.66 < \log g_\star < 4.97$, and $-0.5 < [\mathrm{Fe/H}] < 0.4$. The spectral matching was performed using HPF order index 5 (8534–8645 Å) due to minimal telluric contamination. TOI-3984 A is determined to have $T_e = 3476 \pm 88$ K, $\log g_\star = 4.81 \pm 0.05$, and $[\mathrm{Fe/H}] = 0.18 \pm 0.12$, and TOI-5293 A is determined to have $T_e = 3586 \pm 88$ K, $\log g_\star = 4.77 \pm 0.05$, and $[\mathrm{Fe/H}] = -0.03 \pm 0.12$. The resolution limit of HPF ($R \sim 55{,}000$)

[37] https://neid.ipac.caltech.edu/docs/NEID-DRP/
[38] https://neid.ipac.caltech.edu/
[39] https://gummiks.github.io/hpfspecmatch/

Table 2
Radial Velocities

BJD_{TDB}	RV ($m\ s^{-1}$)	σ ($m\ s^{-1}$)	S/N[a]	Instrument
TOI-3984 A				
2,459,449.620693	0.5	18.2	49	HPF
2,459,451.620722	36.5	20.4	45	HPF
2,459,452.603981	2.5	19.5	47	HPF
2,459,574.028699	−78.2	89.8	34	HPF
2,459,576.029258	−83.2	43.0	34	HPF
2,459,578.027929	−45.0	29.6	34	HPF
2,459,584.013323	49.1	27.5	36	HPF
2,459,597.974678	21.8	31.4	31	HPF
2,459,598.978176	−18.4	33.4	31	HPF
2,459,602.968624	−18.0	24.4	38	HPF
2,459,604.966266	15.5	22.1	43	HPF
2,459,605.946813	9.3	24.7	38	HPF
2,459,606.947872	−50.6	22.7	41	HPF
2,459,623.909836	−56.8	25.1	37	HPF
2,459,624.911946	−41.7	23.8	40	HPF
2,459,626.894567	2.8	28.0	40	HPF
2,459,629.887569	−9.2	24.5	40	HPF
2,459,649.837986	63.6	33.7	40	HPF
2,459,651.825176	−35.1	33.4	40	HPF
2,459,658.810776	−24.1	24.7	40	HPF
2,459,677.769462	69.8	33.9	36	HPF
2,459,677.984824	−10.6	26.6	36	HPF
2,459,678.752641	82.2	26.6	36	HPF
2,459,681.740411	−5.2	32.6	35	HPF
2,459,681.974403	2.1	27.1	35	HPF
2,459,682.749492	−37.4	29.1	35	HPF
2,459,683.749510	44.2	25.2	38	HPF
2,459,683.967863	63.7	29.0	33	HPF
2,459,684.983417	2.2	33.7	30	HPF
2,459,685.974345	−33.1	42.6	38	HPF
2,459,686.729534	7.7	25.5	38	HPF
2,459,687.723023	56.4	25.7	38	HPF
2,459,687.962405	33.6	18.9	49	HPF
2,459,691.942885	1.5	27.9	35	HPF
2,459,709.673097	64.5	20.1	47	HPF
2,459,651.891110	−60.1	12.4	12	NEID
2,459,656.839623	−57.8	9.7	14	NEID
2,459,663.895380	−76.5	7.1	19	NEID
2,459,664.861500	−71.9	11.5	12	NEID
2,459,671.889748	−68.6	14.7	10	NEID
2,459,678.892545	−29.9	9.6	15	NEID
TOI-5293 A				
2,459,846.735412	179.6	37.6	28	HPF
2,459,852.721876	195.1	40.3	27	HPF
2,459,853.718534	−3.3	27.9	36	HPF
2,459,856.709588	−113.7	30.2	35	HPF
2,459,856.779480	−104.9	26.7	38	HPF
2,459,864.686793	52.8	28.8	37	HPF
2,459,865.683293	−98.5	29.9	35	HPF
2,459,873.660887	33.8	25.7	39	HPF
2,459,877.648474	−82.7	40.8	26	HPF
2,459,879.639891	11.6	26.2	38	HPF
2,459,880.642541	−109.4	46.9	23	HPF
2,459,882.640435	48.1	28.5	35	HPF
2,459,885.630585	−10.3	24.6	41	HPF
2,459,890.687347	138.9	25.4	39	HPF
2,459,893.611705	44.1	37.3	29	HPF
2,459,907.568470	56.2	30.1	34	HPF

Note.
[a] The S/N is the median value per 1D extracted pixel at 1070 nm for HPF and 850 nm for NEID. The HPF observations use an exposure time of 1890 s. The NEID observations use an exposure time of 1800 s.

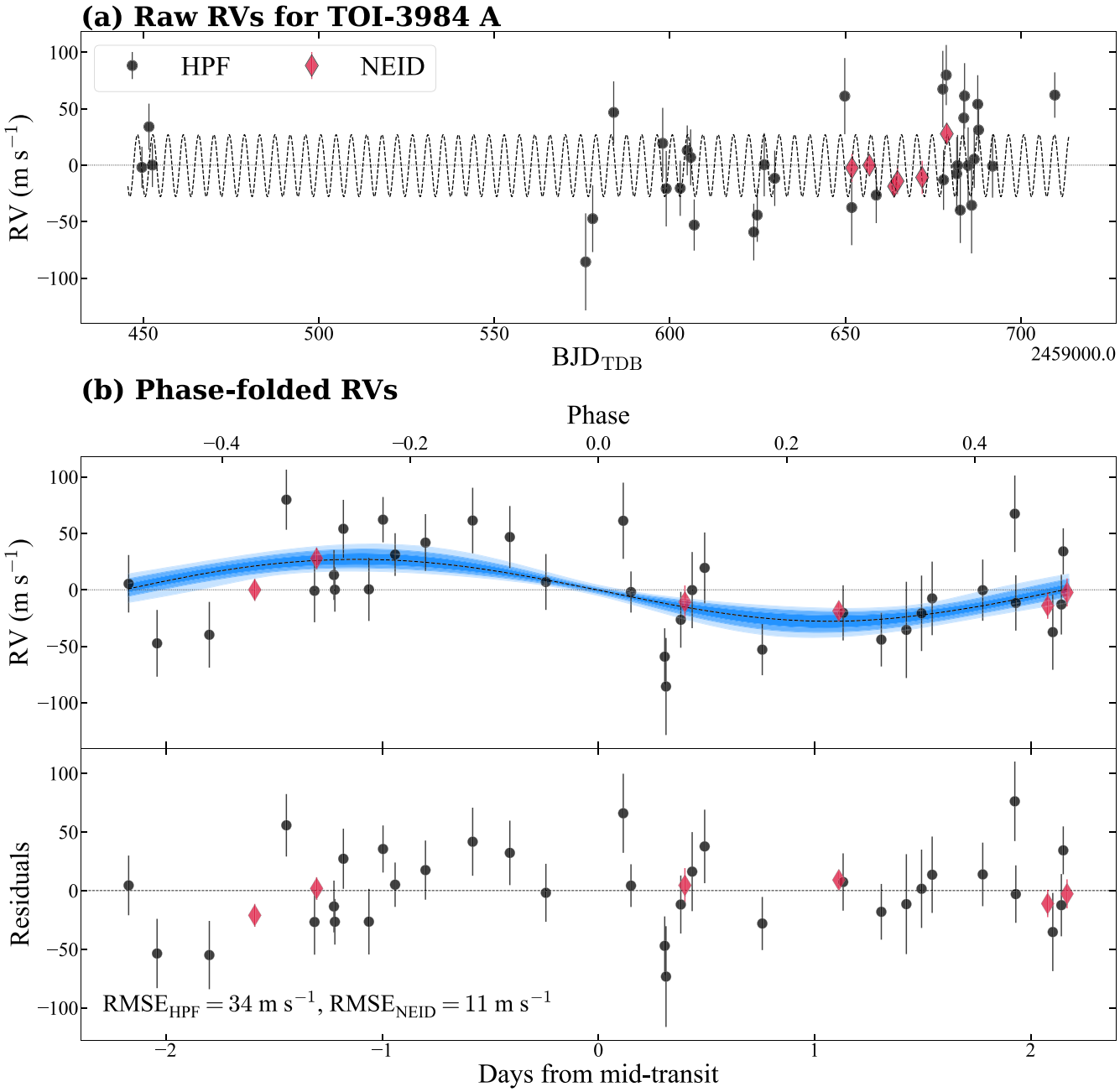

Figure 8. Panel (a) shows the RVs for TOI-3984 A derived with modified versions of SERVAL. Panel (b) displays the phase-folded RVs plotted with model posteriors and the residuals to the fit. In panels (a) and (b), the dashed line is the best-fitting Keplerian model. The shaded regions denote the 1σ (darkest), 2σ, and 3σ (lightest) extent of the model posteriors. The modeling is described in Section 4.

places a constraint of $v \sin i < 2$ km s^{-1} for both TOI-3984 A and TOI-5293 A. Table 3 presents the derived spectroscopic parameters with their uncertainties.

3.2. Spectral Classification

3.2.1. LAMOST

The Large Sky Area Multi-Object Fiber Spectroscopic Telescope (LAMOST) is a 4 m telescope equipped with 4000 fibers distributed over a 5° field of view that is capable of acquiring spectra in the optical band (3700–9000 Å) at $R \approx 1800$ (Cui et al. 2012). TOI-3984 A was observed as part of its spectroscopic survey of the Galaxy (Deng et al. 2012; Yuan et al. 2015; Xiang et al. 2017), while TOI-5293 A has not been observed. The data used in this work are from the public DR8v2.0[40] release (Wang et al. 2022).

The LAMOST stellar classification pipeline uses stellar templates to identify the molecular absorption features (e.g., CaH and TiO) typical for M-type stars (Lépine et al. 2007) and has been shown to report the subclass of an M dwarf with an accuracy of ±0.5 subtypes (Zhong et al. 2015). A successful classification requires that a target have (i) a mean S/N > 5, (ii) a best-matching template that is an M type, and (iii) molecular band indices that are located in the M-type stellar regime

[40] http://dr8.lamost.org/

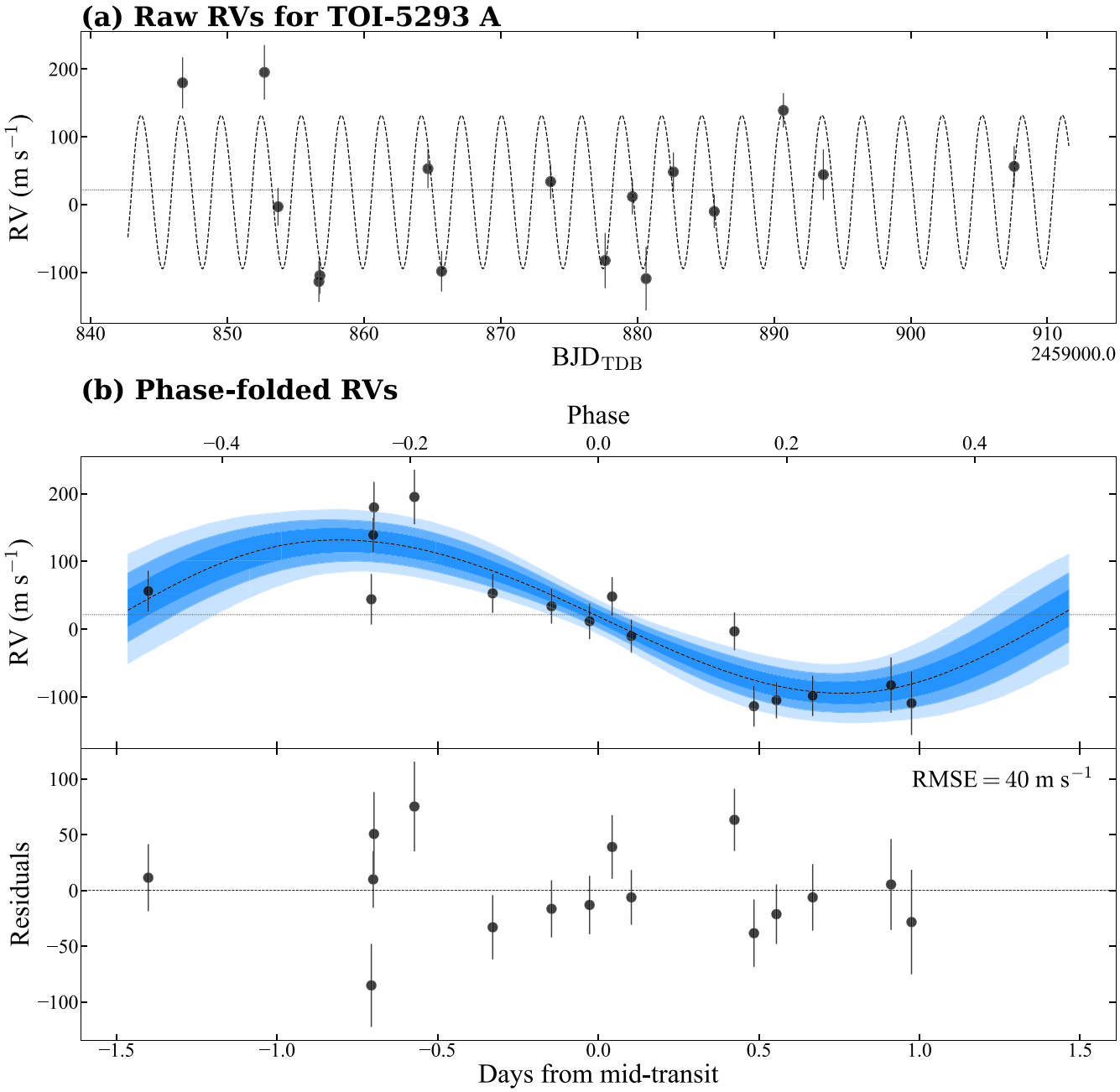

Figure 9. Same as Figure 8 but for TOI-5293 A. Panel (a) shows the HPF RVs. Panel (b) displays the phase-folded RVs plotted with model posteriors.

identified by Zhong et al. (2019; $0 < \mathrm{TiO5} < 1.2$ and $0.6 < \mathrm{CaH2} + \mathrm{CaH3} < 2.4$). LAMOST classifies TOI-3984 A as an M4 $\pm$ 0.5 dwarf, which agrees with the derived parameters in Section 3.1.

3.2.2. LRS2

The second-generation Low Resolution Spectrograph (LRS2; Chonis et al. 2014, 2016) is a low-resolution, optical integral field unit spectrograph on the HET. The LRS2 has broad wavelength coverage spread between two fiber-fed, dual-channel spectrographs that simultaneously observe independent fields separated by 100″. The blue spectrograph pair (LRS2-B) covers 364 nm $\leqslant \lambda \leqslant$ 467 nm and 454 nm $\leqslant \lambda \leqslant$ 700 nm with $R \sim 2500$ and 1400, respectively. The red spectrograph pair (LRS2-R) covers 643 nm $\leqslant \lambda \leqslant$ 845 nm and 823 nm $\leqslant \lambda \leqslant$ 1056 nm at $R \sim 2500$. TOI-5293 A was observed with LRS2-R on 2022 November 1 and LRS2-B on 2022 December 11 using exposure times of 1800 s.

The LRS2 data were processed using the automated pipeline, `Panacea`,[41] and the package `LRS2Multi`.[42] We follow the methodology outlined in Kanodia et al. (2023). Briefly, `Panacea` performs bias correction, wavelength calibration, fiber extraction, and an initial flux calibration, while `LRS2Multi` extracts spectra from `Panacea` products. The stellar spectra are extracted from a 3.″5 aperture centered on TOI-5293 A using sky-subtracted frames. The response correction was derived using calibrated standard stars observed

[41] https://github.com/grzeimann/Panacea
[42] https://github.com/grzeimann/LRS2Multi

Table 3
Summary of Stellar Parameters

Parameter	Description	TOI-3984 A	TOI-5293 A	Reference
Main Identifiers				
TIC	⋯	20182780	250111245	TIC
Gaia DR3	⋯	1291955578869575552	2640121486388076032	Gaia DR3
Coordinates, Proper Motion, Distance, Maximum Extinction, and Spectral Type				
α_{J2016}	R.A.	15:05:20.91	23:43:18.88	Gaia DR3
δ_{J2016}	decl.	36:47:13.14	−02:02:42.33	Gaia DR3
μ_α	Proper motion (R.A., mas yr^{-1})	-48.95 ± 0.02	-17.13 ± 0.03	Gaia DR3
μ_δ	Proper motion (decl., mas yr^{-1})	42.65 ± 0.02	0.49 ± 0.02	Gaia DR3
l	Galactic longitude	60.26769	87.00510	Gaia DR3
b	Galactic latitude	60.17839	−60.07625	Gaia DR3
d	Geometric distance (pc)	$108.4^{+0.3}_{-0.2}$	160.8 ± 0.6	Bailer-Jones
$A_{V,\max}$	Maximum visual extinction	0.04	0.06	Green
Spectral type	⋯	$M4 \pm 0.5$	$M3 \pm 1$	LAMOST/this work[a]
Broadband Photometric Magnitudes				
B	Johnson B mag	⋯	17.4 ± 0.2	APASS
V	Johnson V mag	⋯	15.9 ± 0.2	APASS
g'	Pan-STARRS1 g' mag	16.35 ± 0.02	16.496 ± 0.007	PS1
r'	Pan-STARRS1 r' mag	15.18 ± 0.01	15.29 ± 0.01	PS1
i'	Pan-STARRS1 i' mag	13.96 ± 0.01	14.310 ± 0.008	PS1
z'	Pan-STARRS1 z' mag	13.41 ± 0.02	13.87 ± 0.01	PS1
y'	Pan-STARRS1 y' mag	13.15 ± 0.02	13.657 ± 0.008	PS1
J	J mag	11.93 ± 0.02	12.47 ± 0.03	2MASS
H	H mag	11.32 ± 0.02	11.86 ± 0.03	2MASS
K_s	K_s mag	11.05 ± 0.02	11.64 ± 0.04	2MASS
W1	WISE1 mag	10.94 ± 0.02	11.37 ± 0.02	WISE
W2	WISE2 mag	10.85 ± 0.02	11.30 ± 0.02	WISE
W3	WISE3 mag	10.69 ± 0.06	11.2 ± 0.2	WISE
Spectroscopic Parameters[b]				
T_e	Effective temperature (K)	3476 ± 88	3586 ± 88	This work
$\log g_\star$	Surface gravity (cgs)	4.81 ± 0.05	4.77 ± 0.05	This work
[Fe/H]	Metallicity (dex)	0.18 ± 0.12	-0.03 ± 0.12	This work
$v \sin i_\star$	Rotational broadening (km s^{-1})	<2	<2	This work
Model-dependent Parameters from a Stellar SED and Isochrone Fit[c]				
$M_\star$	Mass ($M_\odot$)	0.49 ± 0.02	0.54 ± 0.02	This work
$R_\star$	Radius ($R_\odot$)	0.47 ± 0.01	$0.52^{+0.02}_{-0.01}$	This work
$\rho_\star$	Density (g cm^{-3})	6.9 ± 0.5	5.4 ± 0.4	This work
A_v	Visual extinction (mag)	0.02 ± 0.01	0.04 ± 0.03	This work
Other Stellar Parameters				
Rotation period	Days	$50.0^{+2.8}_{-2.7}$	$20.6^{+0.3}_{-0.4}$	This work
Age[d]	Gyr	0.7–5.1	0.7–5.1	This work
RV	Systemic RV (km s^{-1})	-5.77 ± 0.06	8.0 ± 0.1	This work
U, V, W	Barycentric Galactic velocities (km s^{-1})	-33.01 ± 0.07, -5.86 ± 0.03, 5.65 ± 0.06	11.56 ± 0.06, 9.63 ± 0.06, -3.32 ± 0.09	This work
$(U, V, W)_{LSR}$	Galactic velocities w.r.t. LSR[e] (km s^{-1})	-21.9 ± 0.8, 6.4 ± 0.5, 12.9 ± 0.4	22.7 ± 0.8, 21.9 ± 0.5, 3.9 ± 0.4	This work

Notes.
[a] The spectral type for TOI-3984 A is from LAMOST DR8. The spectral type for TOI-5293 A is derived with `PyHammer`.
[b] Derived with the `HPF-SpecMatch` package.
[c] Derived with the `EXOFASTv2` package using MIST isochrones.
[d] Ages based on the rotation period and corresponding age range from Newton et al. (2016).
[e] Calculated using the solar velocities from Schönrich et al. (2010).
References. TIC (Stassun et al. 2019), Gaia DR3 (Gaia Collaboration et al. 2022), Bailer-Jones (Bailer-Jones et al. 2021), Green (Green et al. 2019), LAMOST (Zhong et al. 2019), APASS (Henden et al. 2018), PS1 (Chambers et al. 2016), 2MASS (Cutri et al. 2003), WISE (Wright et al. 2010).

between 2021 May and 2022 May, while the telluric correction was constructed using telluric standard stars.

We use `PyHammer` (Kesseli et al. 2017; Roulston et al. 2020) to estimate the spectral type of TOI-5293. `PyHammer` assigns a spectral type by measuring spectral indices for various atomic and molecular lines and comparing the values to those measured from observed stellar templates. The M dwarf templates used by `PyHammer` are from the MaNGA Stellar

Library (362.2–1035.4 nm at $R \sim 1800$; Yan et al. 2019). PyHammer selects the best-matching spectral type by minimizing the χ^2 difference between the spectral indices of the stellar template and observed star. We estimate a spectral type of M3 ± 1 from the LRS2 data, which agrees with the derived parameters in Section 3.1.

3.3. Spectral Energy Distribution Fitting

We modeled the spectral energy distribution (SED; see more details in Appendix A) for each target using the EXOFASTv2 analysis package (Eastman et al. 2019) to derive model-dependent stellar parameters. EXOFASTv2 calculates the bolometric corrections for the SED fit by linearly interpolating the precomputed bolometric corrections[43] in $\log g_\star$, T_e, [Fe/H], and A_V from the MIST model grids (Choi et al. 2016; Dotter 2016). Table 3 contains the stellar priors and derived stellar parameters with their uncertainties. The model-dependent mass and radius are (i) $0.49 \pm 0.02\,M_\odot$ and $0.47 \pm 0.01\,R_\odot$ for TOI-3984 A and (ii) $0.54 \pm 0.02\,M_\odot$ and $0.52^{+0.02}_{-0.01}\,R_\odot$ for TOI-5293 A.

3.4. Stellar Rotation Period

We search the ZTF photometry for a rotation period of any activity-induced photometric modulations in TOI-3984 A and TOI-5293 A using the GLS[44] package. We only consider significant peaks in the periodogram calculated with GLS where the false-alarm probability (FAP), as calculated following Zechmeister & Kürster (2009), is below a threshold of 0.1%. Data within transits were excised using the duration and ephemeris from the QLP. Significant peaks (FAP < 0.1%) of ∼52 were found in both the *zr* and *zg* photometry of TOI-3984 A, while a significant peak of ∼21 days was seen only in the *zr* photometry of TOI-5293 A.

The measured rotation periods are $50.0^{+2.8}_{-2.7}$ days for TOI-3984 A and $20.6^{+0.3}_{-0.4}$ days for TOI-5293 A (see a detailed description of the measurement in Appendix B). These intermediate rotation periods suggest that both TOI-3984 A and TOI-5293 A most likely have ages between 0.7 and 5.1 Gyr if we adopt the classification scheme of Newton et al. (2016). This range is consistent with the estimated rotation periods of ∼3.1 Gyr for TOI-3293 A and ∼1.3 Gyr for TOI-5293 A using the rotation period and age relationship from Engle & Guinan (2018) for M2.5–M6 dwarfs. The age estimates from the model-dependent SED fit of $7.9^{+4.1}_{-5.0}$ and $7.7^{+4.1}_{-4.9}$ Gyr for TOI-3984 A and TOI-5293 A, respectively, are also consistent with the age range from Newton et al. (2016).

3.5. Galactic Kinematics

The *UVW* velocities are derived with galpy (Bovy 2015) and provided with respect to the local standard of rest from Schönrich et al. (2010) using the Gaia DR3 astrometry and the systemic velocity derived from HPF. The values in Table 3 are in a right-handed coordinate system (Johnson & Soderblom 1987) where *UVW* are positive in the directions of the Galactic center, Galactic rotation, and north Galactic pole, respectively. The BANYAN Σ algorithm (Gagné et al. 2018), which uses sky positions, proper motions, parallax, and RVs to constrain cluster membership probabilities, classifies both TOI-3984 A and TOI-5293 A as field stars having no membership in known nearby young associations. Both TOI-3984 A and TOI-5293 A are also classified as members of the thin disk ($P_{\rm thick}/P_{\rm thin} < 0.02$) following the kinematic selection criteria from Bensby et al. (2003).

4. Photometric and RV Modeling

We use the juliet analysis package (Espinoza et al. 2019) to jointly model the RVs with a standard Keplerian RV curve generated from the radvel (Fulton et al. 2018) package and the light curves with a transit model generated from the batman package (Kreidberg 2015). Here juliet performs the parameter estimation using dynesty (Speagle 2020). The photometric model adopts a quadratic limb-darkening law where the coefficients are sampled from uniform priors following the parameterization in Kipping (2013a). For the long-cadence TESS photometry, the transit model utilizes the supersampling option in batman with exposure times of 30 minutes and a supersampling factor of 30.

The TESS photometric model includes a Gaussian process noise model identical to that described in Section 3.4 to account for correlated noise. We do not expect the period of the Gaussian process model to reflect the rotation periods measured in Section 3.4 because the TESS PDCSAP and eleanor CORR_FLUX are generated using algorithms known to attenuate long-period (>10 days) signals (e.g., Van Cleve et al. 2016; Holcomb et al. 2022).

A dilution factor, *D*, is included in the TESS photometric model to account for dilution from nearby stars in the large apertures (see Figures 1 and 2). We assume that the higher spatial resolution and smaller photometric apertures used for the ground-based photometry result in negligible contamination from neighboring stars, such that the dilution term is fixed to unity for all ground-based transits. The fit uses a uniform prior on the TESS dilution term of 0–2 to account for potential overcompensation of the dilution term that can occasionally occur with short-cadence PDCSAP TESS light curves in crowded fields (e.g., Burt et al. 2020). Both the photometric and RV models include a white-noise model parameterized as a jitter term that is added in quadrature to the uncertainty of each data set.

Tables 4 and 5 provide the priors used for the fit along with the inferred system parameters and the confidence intervals (16th–84th percentiles) for TOI-3984 A and TOI-5293 A, respectively. The fits suggest a significant detection of the RV orbit for each system, and we investigate this by comparing the Bayesian information criterion (BIC; Schwarz 1978; Liddle 2007) and the Akaike information criterion (AIC; Akaike 1974). We compute the AIC and BIC of the best-fit RV curve (nine free parameters for the RV curve, five orbital elements and one offset and jitter per instrument) and a flat line (four free parameters, one offset and jitter per instrument) to determine the significance of the detection. We use the likelihood function ($\mathcal{L}$) employed by juliet (Equation (4) in Espinoza et al. 2019) for this comparison. For TOI-3984 A, $\Delta \ln \mathcal{L} = 13.5$, $\Delta{\rm AIC} = 17.1$, and $\Delta{\rm BIC} = 8.4$ between a flat line and a Keplerian model, which provides support for the existence of a Keplerian orbit in the data. Similarly, for TOI-5293 A, $\Delta \ln \mathcal{L} = 46.3$, $\Delta{\rm AIC} = 82.7$, and $\Delta{\rm BIC} = 78.2$ provide very strong evidence for a Keplerian orbit in the data.

Figures 3–5, 8, and 9 display the model posteriors for each system. TOI-3984 A b is a sub-Saturn ($M_p = 0.14 \pm 0.03\,M_{\rm J}$

[43] http://waps.cfa.harvard.edu/MIST/model_grids.html#bolometric
[44] https://github.com/mzechmeister/GLS

Table 4
System Parameters for TOI-3984 A

Parameter	Units	Prior	Value					
Ground-based Photometry Parameters			RBO (07–19)	RBO (08–14)	Soka	RBO (02–04)	ARCTIC (03–23)	ARCTIC (05–10)
Linear limb-darkening coefficient[a]	q_1	$\mathcal{U}(0, 1)$	0.2 ± 0.1	0.2 ± 0.1	$0.09^{+0.03}_{-0.02}$	0.2 ± 0.1	$0.09^{+0.03}_{-0.02}$	$0.05^{+0.03}_{-0.02}$
Quadratic limb-darkening coefficient[a]	q_2	$\mathcal{U}(0, 1)$	0.5 ± 0.2	0.5 ± 0.2	$0.8^{+0.1}_{-0.2}$	0.5 ± 0.2	$0.8^{+0.1}_{-0.2}$	0.6 ± 0.2
Photometric jitter	$\sigma_{\rm phot}$ (ppm)	$\mathcal{J}(10^{-6}, 10^{4})$	$0.0001^{+0.0261}_{-0.0001}$	$0.3^{+20.4}_{-0.3}$	$0.0001^{+0.0045}_{-0.0001}$	$0.02^{+2.35}_{-0.02}$	$0.3^{+24.1}_{-0.3}$	989^{+7}_{-9}
TESS photometry parameters				Long-cadence			Short-cadence	
Linear limb-darkening coefficient[a]	q_1	$\mathcal{U}(0, 1)$		$0.24^{+0.13}_{-0.09}$			$0.24^{+0.13}_{-0.09}$	
Quadratic limb-darkening coefficient[a]	q_2	$\mathcal{U}(0, 1)$		$0.6^{+0.2}_{-0.3}$			$0.6^{+0.2}_{-0.3}$	
Photometric jitter	$\sigma_{\rm phot}$ (ppm)	$\mathcal{J}(10^{-6}, 10^{3})$		$0.01^{+2.56}_{-0.01}$			10^{+80}_{-10}	
Dilution factor	D	$\mathcal{U}(0, 2)$		$0.89^{+0.04}_{-0.03}$			$0.87^{+0.04}_{-0.03}$	
TESS Gaussian Process Hyperparameter								
B	Amplitude (ppm)	$\mathcal{J}(10^{-4}, 10^{12})$		37^{+9}_{-7}			10^{+779}_{-4}	
C	Additive factor	$\mathcal{J}(10^{-3}, 10^{3})$		$0.02^{+0.26}_{-0.01}$			$1.4^{+244.2}_{-1.3}$	
L	Length scale (days)	$\mathcal{J}(10^{-3}, 10^{3})$		$1.7^{+0.6}_{-0.4}$			$1.8^{+133.6}_{-0.8}$	
$P_{\rm GP}$	Period (days)	$\mathcal{J}(1.0, 100)$		$2.7^{+1.2}_{-0.5}$			$2.7^{+1.2}_{-0.5}$	
RV Parameters				HPF			NEID	
Systemic velocity	γ (m s^{-1})	$\mathcal{U}(-10^{3}, 10^{3})$		$2.4^{+4.0}_{-3.8}$			$-57.7^{+10.7}_{-10.4}$	
RV jitter	$\sigma_{\rm RV}$ (m s^{-1})	$\mathcal{J}(10^{-3}, 10^{3})$		$3.1^{+8.0}_{-2.8}$			$29.0^{+14.0}_{-9.8}$	
Orbital Parameters								
Orbital period	P (days)	$\mathcal{N}(4.35, 0.1)$			4.353326 ± 0.000005			
Time of midtransit	T_C (BJD$_{\rm TDB}$)	$\mathcal{N}(2, 459, 715.02, 0.1)$			$2{,}459{,}715.02268 \pm 0.00009$			
$\sqrt{e}\cos\omega$		$\mathcal{U}(-1, 1)$			$-0.07^{+0.23}_{-0.17}$			
$\sqrt{e}\sin\omega$		$\mathcal{U}(-1, 1)$			$-0.05^{+0.09}_{-0.10}$			
Semiamplitude velocity	K (m s^{-1})	$\mathcal{U}(0, 10^{3})$			$27.7^{+5.4}_{-5.0}$			
Scaled radius	$R_p/R_\star$	$\mathcal{U}(0, 1)$			$0.1558^{+0.0009}_{-0.0008}$			
Impact parameter	b	$\mathcal{U}(0, 1)$			$0.18^{+0.06}_{-0.07}$			
Scaled semi-major axis	$a/R_\star$	$\mathcal{J}(1, 100)$			$19.1^{+0.5}_{-0.4}$			
Derived Parameters								
Eccentricity	e	⋯			$0.04^{+0.05}_{-0.03}$, $3\sigma < 0.23$			
Argument of periastron	ω (deg)	⋯			-54^{+189}_{-108}			
Orbital inclination	i (deg)	⋯			89.5 ± 0.2			
Transit duration	T_{14} (hr)	⋯			2.01 ± 0.01			
Mass	M_p ($M_{\rm J}/M_\oplus$)	⋯			$0.14 \pm 0.03/44.0^{+8.7}_{-8.0}$			
Radius	R_p ($R_{\rm J}/R_\oplus$)	⋯			$0.71 \pm 0.02/7.9 \pm 0.24$			
Surface gravity	$\log g_p$ (cgs)	⋯			2.84 ± 0.08			
Density	ρ_p (g cm^{-3})	⋯			$0.49^{+0.11}_{-0.10}$			
Semimajor axis	a (au)	⋯			$0.041^{+0.002}_{-0.001}$			
Average incident flux	$\langle F\rangle$ (10^8 erg s^{-1} cm^{-2} $/S_\oplus$)	⋯			$0.23^{+0.03}_{-0.02}$ $/16.7 \pm 1.8$			
Equilibrium temperature[b]	$T_{\rm eq}$ (K)	⋯			563 ± 15			

Notes.
[a] Using the $q1$ and $q2$ parameterization from Kipping (2013a).
[b] The planet is assumed to be a blackbody, and we ignore heat redistribution.

Table 5
System Parameters for TOI-5293 A

Parameter	Units	Prior	Value				
Ground-based photometry parameters			RBO (07-28)	RBO (09–13)	LCRO	TMMT (10–24)	TMMT (10–27)
Linear limb-darkening coefficient[a]	q_1	$\mathcal{U}(0, 1)$	$0.4^{+0.3}_{-0.2}$	$0.4^{+0.3}_{-0.2}$	0.5 ± 0.2	$0.3^{+0.3}_{-0.2}$	$0.3^{+0.3}_{-0.2}$
Quadratic limb-darkening coefficient[a]	q_2	$\mathcal{U}(0, 1)$	$0.3^{+0.3}_{-0.2}$	$0.3^{+0.3}_{-0.2}$	0.5 ± 0.3	0.3 ± 0.2	0.3 ± 0.2
Photometric jitter	$\sigma_{\rm phot}$ (ppm)	$\mathcal{J}(10^{-6}, 10^3)$	$0.007^{+2.846}_{-0.007}$	$0.04^{+12.96}_{-0.04}$	$0.1^{+34.6}_{-0.1}$	$0.05^{+18.11}_{-0.05}$	$0.2^{+40.7}_{-0.2}$
TESS Photometry Parameters							
Linear limb-darkening coefficient[a]	q_1	$\mathcal{U}(0, 1)$			0.4 ± 0.2		
Quadratic limb- darkening coefficient[a]	q_2	$\mathcal{U}(0, 1)$			0.3 ± 0.2		
Photometric jitter	$\sigma_{\rm phot}$ (ppm)	$\mathcal{J}(10^{-6}, 10^3)$			$0.2^{+37.5}_{-0.2}$		
Dilution factor	D	$\mathcal{U}(0, 2)$			$0.94^{+0.04}_{-0.03}$		
TESS Gaussian Process Hyperparameter							
B	Amplitude	$\mathcal{J}(10^{-10}, 10^6)$			$0.0010^{+0.0015}_{-0.0005}$		
C	Additive factor	$\mathcal{J}(10^{-3}, 10^3)$			$0.2^{+5.5}_{-0.2}$		
L	Length scale (days)	$\mathcal{J}(10^{-3}, 10^3)$			40^{+63}_{-22}		
$P_{\rm GP}$	Period (days)	$\mathcal{J}(1.0, 100)$			16^{+10}_{-5}		
RV Parameters							
Systemic velocity	γ (m s^{-1})	$\mathcal{U}(-10^3, 10^3)$			$21.3^{+10.8}_{-11.4}$		
RV jitter	$\sigma_{\rm RV}$ (m s^{-1})	$\mathcal{J}(10^{-3}, 10^3)$			$27.4^{+12.3}_{-9.8}$		
Orbital Parameters							
Orbital period	P (days)	$\mathcal{N}(2.9, 0.1)$			2.930289 ± 0.000004		
Time of midtransit	T_0 (BJD$_{\rm TDB}$)	$\mathcal{N}(2, 459, 448.9, 0.1)$			$2{,}459{,}448.9148 \pm 0.0004$		
$\sqrt{e}\cos\omega_\star$		$\mathcal{U}(-1, 1)$			$-0.07^{+0.17}_{-0.16}$		
$\sqrt{e}\sin\omega_\star$		$\mathcal{U}(-1, 1)$			-0.17 ± 0.22		
Semiamplitude velocity	K (m s^{-1})	$\mathcal{U}(0, 10^3)$			115.6 ± 14.5		
Scaled radius	$R_p/R_\star$	$\mathcal{U}(0, 1)$			$0.210^{+0.005}_{-0.004}$		
Impact parameter	b	$\mathcal{U}(0, 1)$			$0.32^{+0.12}_{-0.14}$		
Scaled semimajor axis	$a/R_\star$	$\mathcal{J}(1, 100)$			$14.1^{+1.6}_{-1.1}$		
Derived Parameters							
Eccentricity	e	⋯			$0.08^{+0.11}_{-0.06}$, $3\sigma < 0.38$		
Argument of periastron	$\omega_\star$ (deg)	⋯			-92^{+161}_{-45}		
Orbital inclination	i (deg)	⋯			$88.8^{+0.5}_{-0.6}$		
Transit duration	T_{14} (hr)	⋯			$1.94^{+0.05}_{-0.04}$		
Mass	M_p ($M_{\rm J}/M_\oplus$)	⋯			$0.54 \pm 0.07/170.4^{+21.8}_{-21.9}$		
Radius	R_p ($R_{\rm J}/R_\oplus$)	⋯			$1.06 \pm 0.04/11.9 \pm 0.4$		
Surface gravity	$\log g_p$ (cgs)	⋯			$3.11^{+0.12}_{-0.11}$		
Density	ρ_p (g cm^{-3})	⋯			0.56 ± 0.09		
Semimajor axis	a (au)	⋯			$0.034^{+0.004}_{-0.003}$		
Average incident flux	$\langle F\rangle$ (10^8 erg s^{-1} cm^{-2} $/S_\oplus$)	⋯			$0.47^{+0.12}_{-0.09}$ $/34.6^{+8.6}_{-6.2}$		
Equilibrium temperature[b]	$T_{\rm eq}$ (K)	⋯			675^{+42}_{-30}		

Notes.
[a] Using the $q1$ and $q2$ parameterization from Kipping (2013a).
[b] The planet is assumed to be a blackbody, and we ignore heat redistribution.

and $R_p = 0.71 \pm 0.02\,R_{\rm J}$) on a nearly circular orbit with a period of 4.353326 ± 0.000005 days. TOI-5293 A b is a hot Jupiter ($M_p = 0.54 \pm 0.07\,M_{\rm J}$ and $R_p = 1.06 \pm 0.04\,R_{\rm J}$) on a nearly circular orbit with a period of 2.930289 ± 0.000004 days.

We estimate the timescales for circularization using the formalism of Jackson et al. (2008), assuming that the tidal quality factor of each planet spans $Q_p = 10^5$–10^8 based on the observed range from Bonomo et al. (2017), and the tidal quality factor of each host star is $Q_\star = 10^7$ based on the modeling of Gallet et al. (2017). The timescale for circularization spans 0.1–10 Gyr when using the orbit parameters derived from the joint fit. With no precise age or Q_p constraint, these systems may be able to retain a small but nonzero eccentricity. Existing

data are only sufficient to confirm that these are low-eccentricity planetary systems with 3σ upper limits of $e < 0.23$ for TOI-3984 A b and $e < 0.38$ for TOI-5293 A b. Higher-precision photometric observations of the occultation (e.g., Alonso 2018) would be most sensitive to measuring any nonzero eccentricity.

5. Discussion

5.1. The Dynamical Implication of Wide-separation Companions

Hot Jupiters are difficult to form in situ at their observed separations from host stars (e.g., Dawson & Johnson 2018; Anderson et al. 2020; Poon et al. 2021) either through gravitational instability (e.g., Boss 1997; Durisen et al. 2007) or core accretion (e.g., Perri & Cameron 1974; Pollack et al. 1996; Chabrier et al. 2014). These systems are hypothesized to have migrated from larger distances via the loss of angular momentum due to gravitational interactions with the circumstellar gas disk (e.g., Goldreich & Tremaine 1980; Lin & Papaloizou 1986; Lin et al. 1996; Ida & Lin 2008; Baruteau et al. 2014) or other massive companions (e.g., Rasio & Ford 1996; Weidenschilling & Marzari 1996; Wu & Murray 2003; Fabrycky & Tremaine 2007; Petrovich 2015a, 2015b). Gas disk migration predominantly results in circular planetary orbits that are well aligned with the spin axis of the host star, while high-eccentricity tidal migration preferentially results in planets on misaligned and eccentric orbits that may have large-separation companions.

We search for wide companions using a list of spatially resolved binary stars from an analysis of proper motions in Gaia EDR3 (El-Badry et al. 2021). Wide-separation binary systems in El-Badry et al. (2021) are flagged as having either a main-sequence or white dwarf companion using the location of the companion on the Gaia color–absolute magnitude diagram (El-Badry & Rix 2018). TOI-3984 A has a white dwarf companion, Gaia DR3 1291955574574621056 (TIC 1101522311), at a projected distance of $3\farcs27$ or a projected separation of 356 au. TOI-5293 A has an M dwarf companion, Gaia DR3 2640121482094497024 (TIC 2052711961), at a projected distance of $3\farcs57$ or a projected separation of 579 au. The companions have a negligible probability ($<4 \times 10^{-8}$; see a detailed description in Appendix A of El-Badry et al. 2021) of being a false detection as a result of chance alignment with a background source having spurious parallax and proper-motion measurements. The NEID and HPF spectra are not contaminated by either companion, as they lie outside the HPF ($\sim 1\farcs7$ on-sky; Kanodia et al. 2018) and NEID HR ($\sim 0\farcs9$ on-sky; Schwab et al. 2016) fibers.

We use `phot_bp_rp_excess_factor` to determine if any of the measured blue or red Gaia photometry of either bound companion is blended or contaminated (Evans et al. 2018b; Riello et al. 2021). The value of `phot_bp_rp_excess_factor` in the Gaia DR3 archive is known to have a strong color dependence, and the Gaia documentation suggests using a corrected excess factor that compares the reported value to the expected excess factor at a given color as derived from sources with good-quality photometry (see the discussion in Section 6 of Riello et al. 2021). We calculate a corrected `phot_bp_rp_excess_factor`[45] of 0.20 and 0.15 for TOI-3984 B and TOI-5923 B, respectively. The deviation from zero reveals that both companions have some contamination in their Gaia colors. We adopt these colors as nominal values to qualitatively characterize the wide-separation companions but note that the photometry and spectroscopy of each target is required to provide robust companion parameters.

The Gaia General Stellar Parameterizer from Photometry (GSP-Phot) algorithm (Andrae et al. 2022) confirms that (i) the companion to TOI-3984 A is most likely a white dwarf based on its location on the Gaia color–magnitude diagram and (ii) the companion to TOI-5293 A is a main-sequence M dwarf. TOI-5293 B is reported to be a mid-M dwarf with a radius of $R_\star = 0.26^{+0.10}_{-0.08}\,R_\odot$ (Creevey & Lebreton 2022; Creevey et al. 2022) and $\log g = 4.72^{+0.16}_{-0.14}$ and $T_e = 3041^{+280}_{-41}$ K derived by the Gaia DR3 Multiple Star Classifier[46] (MSC) analysis of Gaia BP/RP spectra.

Neither GSP-Phot nor MSC provide stellar parameters for TOI-3984 B, and we use the `WD_models`[47] package from Cheng et al. (2019) to derive a photometric age and mass. We assume that the atmosphere is composed of hydrogen due to the prevalence of DA white dwarfs in the 100 pc SDSS sample ($\sim$65% of the sample; Kilic et al. 2020; Kepler et al. 2021) and adopt the cooling models of Bédard et al. (2020). The estimated mass for the white dwarf companion is $M_{\rm WD} \sim 0.75\,M_\odot$ with a cooling age of $\sim$2.9 Gyr (see Appendix C), and its progenitor star has a mass in the range of 1.6–4.5 $M_\odot$ when using the MIST semiempirical white dwarf initial–final mass relationship from Cummings et al. (2018). We note that the cooling age is consistent with the age estimate of TOI-3984 A from the rotation period in Section 3.4 (0.7–5.1 Gyr).

Various studies have been performed on the hot Jupiter population orbiting Sun-like stars to test the significance of multibody interactions (e.g., Knutson et al. 2014; Wang et al. 2014; Ngo et al. 2015; Madhusudhan 2016; Evans et al. 2018a; Ziegler et al. 2018; Fontanive et al. 2019; Marzari & Thebault 2019; Belokurov et al. 2020; Hwang et al. 2020; Fontanive & Bardalez Gagliuffi 2021; Ziegler et al. 2021). Hot Jupiters orbiting Sun-like stars have been reported to have a high wide binary fraction relative to field stars. Madhusudhan (2016) measured that $47\% \pm 7\%$ of systems with a hot Jupiter have resolved stellar companions between separations of 50 and 2000 au, while Fontanive et al. (2019) determined that $79.0^{+13.2}_{-14.7}\%$ of systems with a massive substellar object have a wide companion between 20 and 10000 au. Moe & Kratter (2021) reassessed these claims by accounting for biases and selection effects in the sample to conclude that wide-separation companions (50–2000 au) to hosts of hot Jupiters do not enhance the formation of hot Jupiters at a statistically significant level and that the larger wide binary fraction of hot Jupiters is a result of suppressed hot Jupiter formation in close binaries. This nonenrichment in wide-separation companions has been observed in the hot Jupiter population orbiting Sun-like stars with Gaia (Hwang et al. 2020).

The small population of hot Jupiters orbiting M dwarfs precludes an extensive study of stellar companions. Only two additional M dwarfs in the existing population of 10 transiting hot Jupiters ($P < 10$ days, $R_p > 8\,R_\oplus$), HATS-74A (Jordán et al. 2022) and TOI-3714 (Cañas et al. 2022), are known to have wide-separation companions. HATS-74A has an M dwarf

[45] Using Table 2 and Equation (6) from Riello et al. (2021).

[46] https://gea.esac.esa.int/archive/documentation/GDR3/Data_analysis/chap_cu8par/sec_cu8par_apsis/ssec_cu8par_apsis_msc.html

[47] https://github.com/SihaoCheng/WD_models

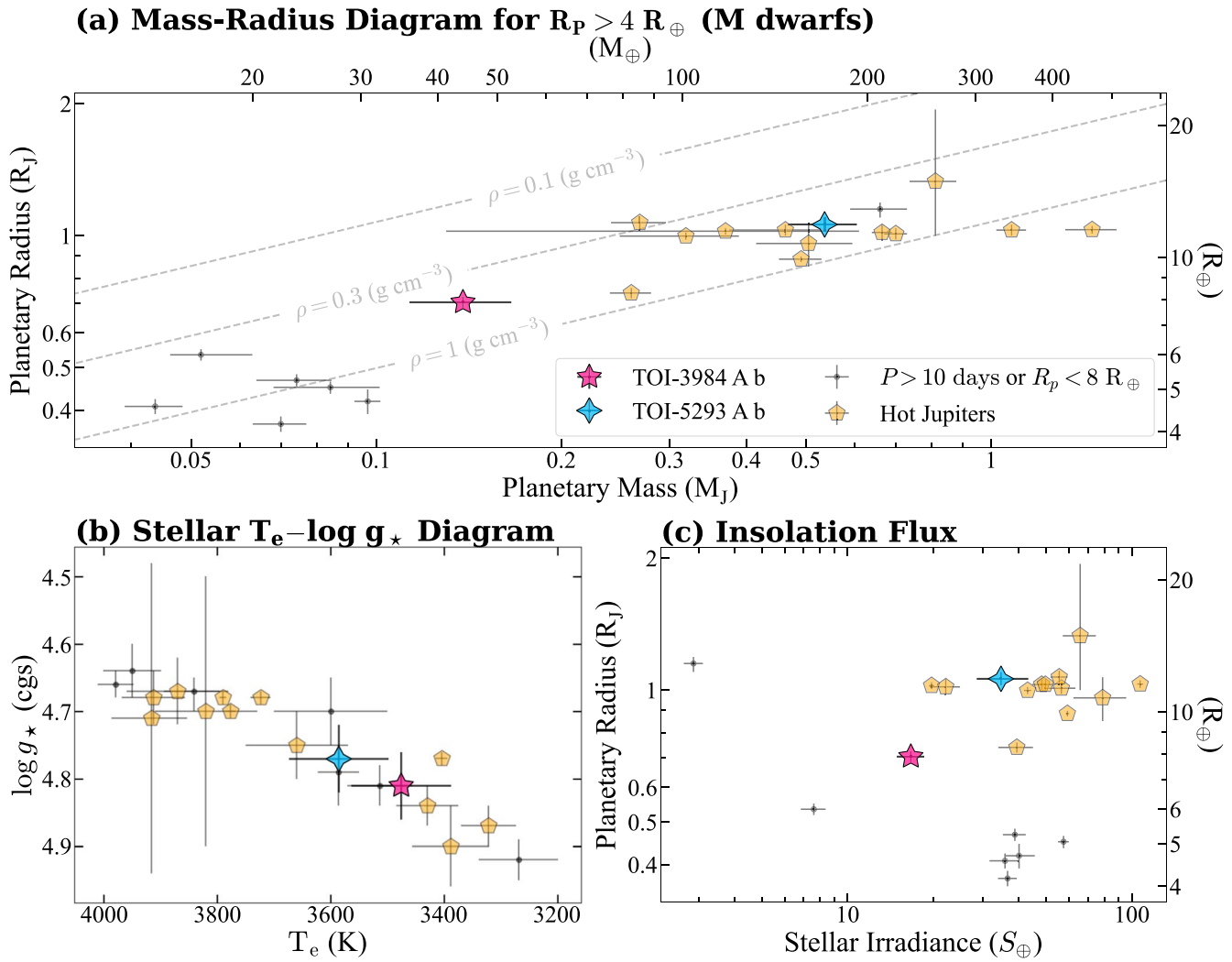

Figure 10. (a) TOI-3984 A b (star) and TOI-5293 A b (diamond star) on the mass–radius diagram for transiting M dwarf exoplanets with mass measurements and $R_p > 4\ R_\oplus$. All previously known hot Jupiters ($P < 10$ days and $R_P \geqslant 8\ R_\oplus$) transiting M dwarfs are marked as pentagons. (b) TOI-3984 A and TOI-5293 A on an effective temperature–surface gravity diagram. (c) Insolation flux and radius for these planets. The data were compiled from the NASA Exoplanet Archive (Akeson et al. 2013) on 2023 May 3.

companion at a separation of 238 au, while TOI-3714 has a white dwarf companion, potentially on an eccentric orbit, at a projected separation of 302 au.

The separation of the main-sequence companions may be too large to strongly impact the formation of hot Jupiters, as some studies suggest that only companions at separations of $\lesssim$200 au can impact the formation process (e.g., Kraus et al. 2016; Moe & Kratter 2021; Ziegler et al. 2021). The white dwarf progenitor in the TOI-3984 A system, however, would have been both more massive and much closer if we assume adiabatic mass loss (see Nordhaus et al. 2010; Nordhaus & Spiegel 2013), and during the progenitor's main-sequence lifetime, secular effects such as Kozai–Lidov cycles (Kozai 1962; Lidov 1962; Naoz 2016) could have induced high-eccentricity tidal migration of TOI-3984 A b that brought it to its observed location.

Gaia DR3 is able to constrain the eccentricity of resolved wide binaries (e.g., Tokovinin 2020; Hwang et al. 2022) using the angle between the separation vector and the relative velocity vector (v–r angle). Hwang et al. (2022) estimated the eccentricity of the wide binary sample identified by El-Badry et al. (2021) under the assumption that a wide companion has a random orbital orientation. The inferred eccentricities calculated by Hwang et al. (2022) are $e = 0.64^{+0.18}_{-0.26}$ and $0.77^{+0.16}_{-0.24}$ for TOI-3984 B and TOI-5293 B, respectively.

Similar to the white dwarf companion to TOI-3714, the high eccentricity of TOI-3984 B is consistent with the scenario in which the progenitor star was initially on a smaller orbit, potentially inducing the migration of TOI-3984 A b, before later widening and becoming eccentric due to mass loss as it evolved into a white dwarf. While TOI-5293 B is also eccentric, the large projected separation (579 au) would result in a >5 Gyr timescale for the Kozai–Lidov cycles (Equation (7) from Kiseleva et al. 1998), which would be too long to affect the migration of TOI-5293 A b, particularly given the most likely age of 0.7–5.1 Gyr derived in Section 3.4.

5.2. Constraints on Additional Planetary Companions

There are 15 confirmed planetary systems hosting a close-in gas giant ($P < 100$ days and $M > 0.6\ M_J$) with interior companions across all spectral types (see Table A1 in Sha et al. 2023). For the transiting hot Jupiter sample ($P < 10$ days), there are only six confirmed gas giants with nearby

companions: WASP-47 b (Becker et al. 2015), Kepler-730 b (Zhu et al. 2018; Cañas et al. 2019), TOI-1130c (Huang et al. 2020c), WASP-148 b (Wang et al. 2022), WASP-132 b (Hord et al. 2022), and TOI-2000 (Sha et al. 2023). This low planetary multiplicity rate for hot Jupiters orbiting Sun-like stars has been statistically confirmed with multiple ground- and space-based transiting samples (e.g., Steffen et al. 2012; Huang et al. 2016; Maciejewski 2020; Hord et al. 2021; Wang et al. 2021; Zhu & Dong 2021). A search for transit timing variations in the Kepler sample by Wu et al. (2023) also determined that a minimum of ∼13% of hot Jupiters orbiting Sun-like stars have nearby companions and must have a quiescent formation history. The scarcity of short-period companions to hot Jupiters is consistent with the hypothesis that high-eccentricity migration is responsible for most of these systems, as the inward migration of a gas giant is a dynamically "hot" process that would destabilize interior planets and leave an isolated gas giant (e.g., Mustill et al. 2015; Dawson & Johnson 2018).

We search for companions to TOI-3984 A and TOI-5923 using the available TESS photometry and HPF RVs. We used the transit least-squares algorithm (TLS; Hippke & Heller 2019) on the photometry to search for additional transiting planets after subtracting the best-fitting transit model for each planet. For this search, we only searched for candidate signals (depths >1 ppm) between 1 and 13 days. The maximum radius of a candidate signal was $\sim 5\,R_\oplus$ for TOI-3984 A and $\sim 7\,R_\oplus$ for TOI-5293 A. The TLS identified no candidates where the test statistic was above the suggested threshold of 7 (corresponding to a false-positive rate of 1%). The current TESS photometry is only sufficient to exclude the existence of additional short-period transiting gas giant companions.

To further constrain the existence of nontransiting companions, we analyzed the residuals to the HPF RVs using `thejoker` (Price-Whelan et al. 2017) to perform a rejection sampling analysis. Orbits were sampled using a log-uniform prior for the period (between 1 day and twice the HPF RV baseline), the beta distribution from Kipping (2013b) as a prior for the eccentricity, and a uniform prior for the argument of pericenter and the orbital phase. We considered a total of 2^{28} samples using `thejoker` and had a total acceptance rate of <0.07% for both systems. The surviving samples place a 3σ upper limit on any coplanar ($\sin i \sim 1$) companions of $M < 2.4\,M_J$ ($K < 150\,\mathrm{m\,s^{-1}}$) within 1 au ($P < 520$ days) for TOI-3984 A[48] and $M < 0.6\,M_J$ ($K < 100\,\mathrm{m\,s^{-1}}$) within 0.3 au ($P < 82$ days) for TOI-5293 A. The existing photometry and RVs reject the existence of nearby, coplanar massive planetary companions. Future observations with TESS and additional RVs are needed to provide robust constraints on the existence of small and low-mass transiting or nontransiting planetary companions.

5.3. Comparison to the M Dwarf Planet Population

A comparison of the TOI-3984 A and TOI-5293 A systems to the planetary mass–radius, stellar $T_e - \log g_\star$, and period–insolation flux distributions of known M dwarf systems hosting planets with $R_p > 4\,R_\oplus$ is shown in Figure 10. Among the population of short-period gas giants ($P < 10$ days and $R_p \gtrsim 8\,R_\oplus$) orbiting M dwarfs, TOI-3984 A b is a sub-Saturn with the smallest mass ($\sim 0.47\,M_{\mathrm{Saturn}}$) and radius ($\sim 0.88\,R_{\mathrm{Saturn}}$), while TOI-5293 A has a radius and mass consistent at 1σ with the median values of the existing M dwarf gas giant population ($1.02\,R_J$ and $0.50\,M_J$). The mid-M dwarf nature of the host stars makes these two planets some of the coolest transiting M dwarf gas giants with an insolation flux of $S = 16.7 \pm 1.8\,S_\oplus$ for TOI-3984 A and $S = 34.6^{+8.6}_{-6.2}\,S_\oplus$ for TOI-5293 A, much lower than the typical transiting M dwarf gas giant (median value of $S \sim 56\,S_\oplus$).

There are two additional hot Jupiters orbiting mid-M dwarfs (M3–M5, $3400\,\mathrm{K} < T_e < 3600\,\mathrm{K}$), HATS-71 b (Bakos et al. 2020) and TOI-5205 b (Kanodia et al. 2023), while the rest orbit early M dwarfs (M0–M2). The frequency of such hot Jupiters orbiting M dwarfs is theoretically predicted to be intrinsically low in the framework of core accretion because the low surface density of an M dwarf protoplanetary disk would impede the growth of cores and the onset of runaway gas accretion (e.g., Laughlin et al. 2004; Ida & Lin 2005; Kennedy & Kenyon 2008; Burn et al. 2021). Constraints from RV (e.g., Endl et al. 2006; Sabotta et al. 2021; Pinamonti et al. 2022) and photometric (e.g., Kovács et al. 2013; Obermeier et al. 2016) surveys have constrained the frequency of short-period gas giants orbiting M dwarfs to $\lesssim$2%. Two independent searches for hot Jupiters orbiting M dwarfs in TESS by Gan et al. (2023) and Bryant et al. (2023) have yielded an occurrence rate of $0.27\% \pm 0.09\%$ and $0.193\% \pm 0.072\%$, respectively.

The measured occurrence rates for M dwarfs are smaller than the recent values measured from TESS for Sun-like stars of $0.71\% \pm 0.31\%$ (Zhou et al. 2019) and $0.98\% \pm 0.36\%$ (Beleznay & Kunimoto 2022). For comparison, the occurrence rate of hot Jupiters orbiting Sun-like stars has consistently been estimated to be ∼1% from various RV surveys, such as the California Planet Survey ($1.2\% \pm 0.38\%$; Wright et al. 2012), the HARPS/CORALIE survey ($0.9\% \pm 0.4\%$; Mayor et al. 2011), and the Anglo-Australian Planet Search ($0.84^{+0.7}_{-0.2}\%$; Wittenmyer et al. 2020). Results from the California Legacy Survey (Zhu 2022) suggest a higher occurrence rate of $2.8\% \pm 0.8\%$, but Zhu (2022) warned that the differences in the stellar population (such as binarity and metallicity) may result in a discrepancy from the canonical ∼1% occurrence rate for Sun-like stars. The current results for M dwarfs from Gan et al. (2023) and Bryant et al. (2023) suggest that hot Jupiters are rarer as companions to M dwarfs, but these values are also within 1σ–3σ of most occurrence rates for Sun-like stars.

The apparent dearth of hot Jupiters orbiting M dwarfs is expected if they predominantly form via core accretion. Giant planet formation must occur before depletion of the gas disk. The low mass and surface density of protoplanetary disks around M dwarfs (e.g., Andrews et al. 2013; Mohanty et al. 2013; Stamatellos & Herczeg 2015; Ansdell et al. 2017; Manara et al. 2018) stymie this process with a lower mass supply and longer timescales of planetesimal formation (Laughlin et al. 2004). While the preference for hot Jupiters to orbit early M dwarfs may be an observational bias or a result of a small population size, the efficiency and prevalence of gas giants should increase when orbiting more massive M dwarfs.

5.4. Comparison to Planetary Models

These planets are unlikely to exhibit any radius inflation due to stellar flux-driven mechanisms. Studies of the Kepler population of transiting hot Jupiters (e.g., Thorngren & Fortney 2018; Thorngren et al. 2021) show that inflated radii are only evident when $T_{\mathrm{eq}} > 1000$ K or the incident flux is $> 2 \times 10^8\,\mathrm{erg\,s^{-1}\,cm^{-2}}$. These values serve as the threshold for

[48] For comparison, $M < 0.5\,M_J$ within 0.3 au.

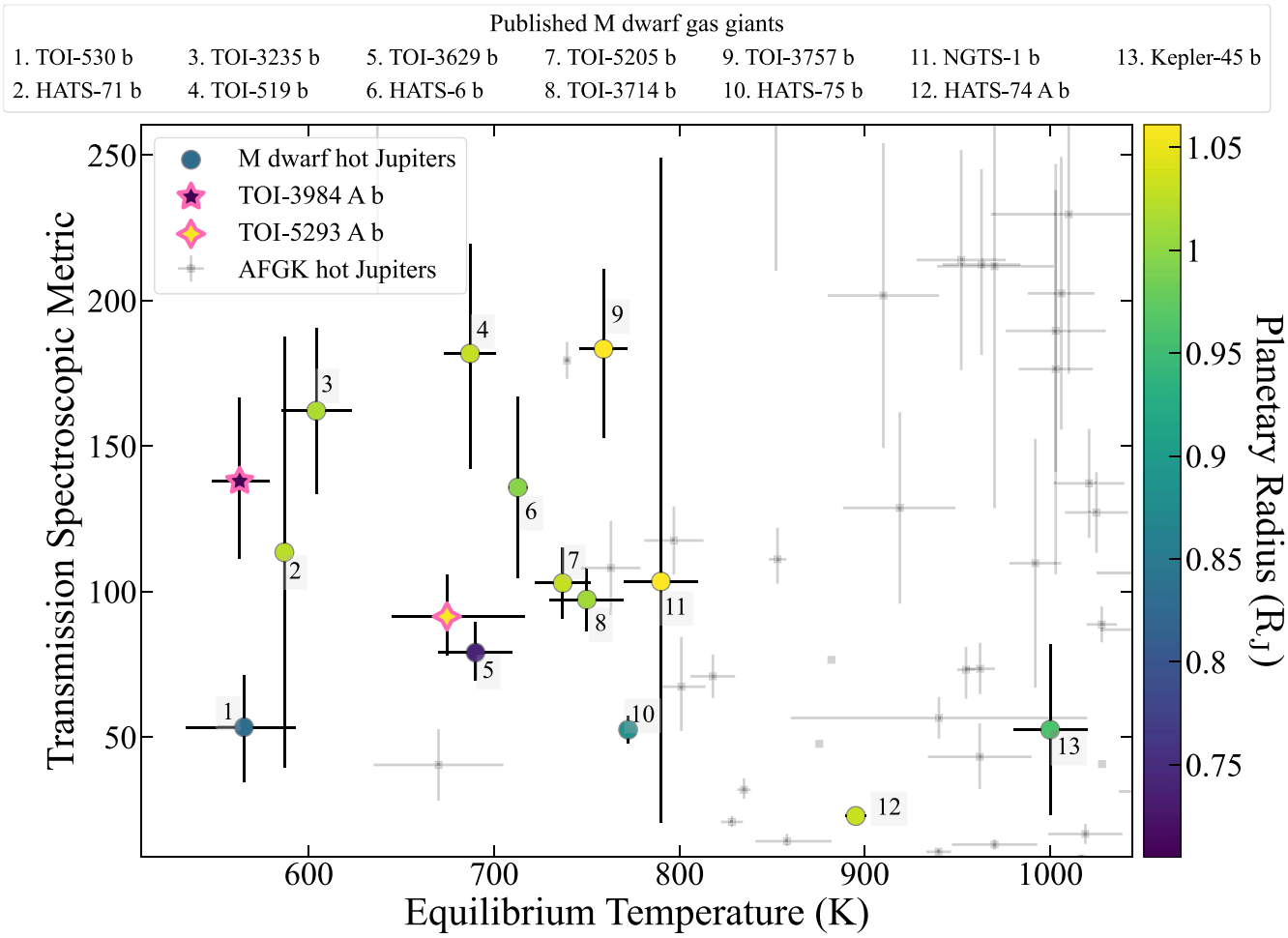

Figure 11. Comparison of the TSM from Kempton et al. (2018) for TOI-3984 A and TOI-5293 A to the existing M dwarf gas giant population ($P < 10$ days and $R_p > 8$ R_J). TOI-3984 A is the coolest object in this sample and provides an opportunity to characterize the chemistry in a gas giant with $T_{eq} < 600$ K. TOI-5293 A b overlaps with TOI-3629 b in equilibrium temperature and TSM but is much larger in radius and provides an opportunity to study a temperate gas giant with $R > 1$ R_J. The TSM value for hot Jupiters orbiting Sun-like stars is included for reference. The data were compiled from the NASA Exoplanet Archive on 2023 May 3.

the apparent radius anomaly of hot Jupiters, where some planets have radii much larger than expected for a pure hydrogen and helium Jovian analog (see Fortney et al. 2021, and references therein).

The mass and radii for TOI-3984 A and TOI-5293 A are within 2σ–3σ of the predicted values from models for gas giants between 1 and 5 Gyr by Baraffe et al. (2008), which assume a gaseous hydrogen and helium envelope with a distribution of heavy elements, and Fortney et al. (2007), which assume a solar metallicity hydrogen and helium atmosphere with a heavy-element core composed of a 50/50 mixture of ice and rock. We compared TOI-3984 A b and TOI-5293 A b to the predicted mass and radii for a solar metallicity atmosphere and noted agreement in the mass and radius within 2σ–3σ regardless of age. For TOI-3984 A b, the models of Baraffe et al. (2008) suggest a large heavy-element fraction ($Z = M_{env}/M_p \approx 0.3$–$0.5$), while the Fortney et al. (2007) models similarly suggest a core 0.25–0.55 times the planetary mass. It may be possible that the apparent upper limit for Z is large because we ignore the effects of tidal heating. Through a population study of sub-Saturns, Millholland et al. (2020) determined that ignoring radius inflation due to tides driven by a nonzero eccentricity or obliquity would result in $Z \gtrsim 0.5$. The younger models favor a larger Z, but the poor constraints on age and eccentricity preclude a detailed study of tidal heating in TOI-3984 A. In comparison, the mass and radius of TOI-5293 A are typical of a canonical Jupiter and consistent with models from Fortney et al. (2007) having no core or the Baraffe et al. (2008) models with a negligible heavy-element fraction of $Z = 2\%$.

5.5. Future Characterization

5.5.1. Stellar Obliquity

Measurements of the projected obliquity (λ), or the angle between a star's spin axis and the orbit normal of a companion, have been useful to constrain the physical processes responsible for the observed planetary architectures (see the reviews by Triaud 2018 and Albrecht et al. 2022). Studies of the obliquities of hot Jupiters orbiting Sun-like stars have revealed an obliquity distribution that is consistent with a formation process involving high-eccentricity migration and tidal damping (e.g., Albrecht et al. 2012; Rice et al. 2022).

Obliquity measurements for M dwarf systems are rarer due to the faintness of the host stars, and only a handful of M dwarf systems have obliquity measurements: GJ 436 (Bourrier et al. 2018, 2022), K2-25 (Stefánsson et al. 2020b), GJ 3740 (Stefánsson et al. 2022), TRAPPIST-1 (Hirano et al. 2020a; Brady et al. 2023), and AU Mic (Hirano et al. 2020b;

Palle et al. 2020; Addison et al. 2021). Of these, GJ 436 b and GJ 3470 b are observed to be on polar orbits, while the other systems are observed to be on well-aligned orbits. Due to the rarity and relative faintness of M dwarfs hosting gas giants, there is no measurement of λ for such a system, and it is not known if high-eccentricity migration coupled with tidal damping is also the dominant formation pathway for these planets.

Both TOI-3984 A and TOI-5293 A have a measured rotation period (see Section 3.4), which allows for constraints on the 3D obliquity, ψ (e.g., Stefánsson et al. 2022; Frazier et al. 2023). A measurement of ψ for exoplanets across all spectral types has revealed that these planets do not span the full range of ψ but tend to be either polar or well aligned, which may be a remnant of formation and not due to tidal evolution (Albrecht et al. 2021; Spalding & Winn 2022). Measurements of ψ for M dwarf gas giants are required to investigate if the distribution is also bimodal for this population.

We estimate the amplitude of the RV anomaly due to the Rossiter-Mclaughlin effect (Equation (1) in Triaud 2018) for both stars using the derived transit and stellar parameters. We derive an equatorial velocity of $v_{\rm eq} = 0.47 \pm 0.03$ km s^{-1} and RM amplitude of $\sim$8 m s^{-1} for TOI-3984 A. For TOI-5293 A, $v_{\rm eq} = 1.28^{+0.06}_{-0.04}$ km s^{-1} with an RM amplitude of $\sim$36 m s^{-1}. The precision to detect these signals around faint ($V = 16$–17) M dwarfs can be achieved using current high-resolution spectrometers on large telescopes, such as MAROON-X (Seifahrt et al. 2016) or KPF (Gibson et al. 2016).

5.5.2. Transmission Spectroscopy

Understanding the atmospheric composition of an exoplanet is important to determine its bulk planetary composition and provide constraints on internal structure models (see the reviews by Madhusudhan 2019; Fortney et al. 2020), which can then be linked to formation and evolutionary processes. Theoretical studies have predicted that key volatile molecules, such as H_2O, CH_4, and CO, should be present in the hydrogen-dominated atmospheres of hot Jupiters at high temperatures (e.g., Burrows & Sharp 1999; Moses et al. 2011; Madhusudhan 2012). Current and future atmospheric missions, such as JWST (Greene et al. 2016) and ARIEL (Tinetti et al. 2018), will characterize such gas giants over a wide range of temperatures to adequately sample a wide range of transitions in atmospheric chemistry (Madhusudhan et al. 2011; Mollière et al. 2015; Fortney et al. 2020).

Beyond the detection of individual species, atmospheric abundances can be used to estimate the C/N/O ratios, which in turn are thought to trace where within the protoplanetary disk a planet forms (Öberg et al. 2011; Madhusudhan 2012; Öberg & Wordsworth 2019; Turrini et al. 2021; Hobbs et al. 2022). Current attempts to constrain migration processes from atmospheric composition have had limited success, and a more detailed characterization of exoplanet atmospheres would help inform planet formation models (e.g., Dash et al. 2022; Mollière et al. 2022).

In the context of hot Jupiters orbiting Sun-like stars, studies with HST have revealed a diverse sample containing both cloudy and clear planets with depleted water abundance relative to predictions from the solar system (e.g., Sing et al. 2016; Pinhas et al. 2019; Welbanks et al. 2019). No studies have been performed on M dwarf hot Jupiters to date. TOI-3984 A b and TOI-5293 A b have the precision of mass and radius ($>5\sigma$) required for detailed atmospheric analysis (Batalha et al. 2019). The large transmission spectroscopy metric (TSM; Kempton et al. 2018) of both TOI-3984 A b (TSM $= 138^{+29}_{-27}$) and TOI-5293 A b (TSM $= 92 \pm 14$) make these favorable targets among the M dwarf gas giant population to be observed with JWST, as shown in Figure 11. While these planets do not have the highest TSM among the M dwarf gas giants (TOI-3757 has a TSM $= 180 \pm 30$), they are unique in the population due to their cooler equilibrium temperature. Almost all of the corresponding hot Jupiters orbiting Sun-like stars are hotter than TOI-3984 A b and TOI-5293 A b or have lower TSMs.

An important factor in understanding exoplanetary atmospheres is the prevalence of clouds and hazes, which may form in the hot Jupiters through condensation chemistry or photochemical processes (e.g., Sudarsky et al. 2003; Helling et al. 2008; Marley et al. 2013). The presence of clouds or hazes can impact atmospheric processes and weaken or mask spectral features (e.g., Sing et al. 2016; Sing 2018). Numerous theoretical studies have predicted the ubiquity of clouds in atmospheres at all temperatures (Marley & Robinson 2015; Gao et al. 2021). Disequilibrium processes are thought to be more efficient in the atmospheres of cooler exoplanets like TOI-3984 A b and TOI-5293 A b (e.g., Moses et al. 2011), and the production of aerosols may be enhanced due to the higher percentage of total UV energy from M dwarfs compared to Sun-like stars (e.g., Liang et al. 2004; Line et al. 2010; Youngblood et al. 2016; Melbourne et al. 2020). Transmission spectra with JWST using NIRSpec would provide the ample wavelength coverage needed to make comparisons to predictions from cloud and haze models (e.g., Kawashima et al. 2019; Mai & Line 2019) and the effects of a higher UV radiation environment of early M dwarfs on atmospheric chemistry (e.g., Pineda et al. 2021).

6. Summary

We present and characterize two gas giants orbiting mid-M dwarfs. TOI-3984 A b is a short-period sub-Saturn ($M_p = 0.14 \pm 0.03\,M_{\rm J}$ and $R_p = 0.71 \pm 0.02\,R_{\rm J}$) on a $P = 4.353326 \pm 0.000005$ day orbit. TOI-5293 A b is a hot Jupiter ($M_p = 0.54 \pm 0.07\,M_{\rm J}$ and $R_p = 1.06 \pm 0.04\,R_{\rm J}$) on a $P = 2.930289 \pm 0.000004$ day orbit. Both systems have measured rotation periods between 10 and 70 days and probably have ages between 0.7 and 5.1 Gyr. They are in wide-separation binary systems, with TOI-3984 A having a white dwarf companion at a projected separation of 356 au and TOI-5293 A having a later-type M dwarf companion at a projected separation of 579 au. For TOI-3984 A, the age range estimated from the rotation period is in agreement with the nominal cooling age of its white dwarf companion ($\sim$2.9 Gyr), which may have once been close enough to impact the migration of TOI-3984 A b. The companion to TOI-5293 A is too far to impact the migration of its planet. Existing photometric and RV data are sufficient to reject the presence of additional massive, close-period planetary companions in these systems. TOI-3984 A b has the smallest mass and radius among the current sample of M dwarf gas giants, while TOI-5293 A b is a typical M dwarf gas giant and consistent with the median mass and radius of the existing population. These two planets are, however, much cooler than the typical M dwarf gas giants due to the mid-M dwarf nature of the host stars. TOI-3984 A b and TOI-5293 A b are bright enough to facilitate

observations during transit to (i) further our understanding of their dynamical history with a measurement of the projected and 3D obliquities (λ and ψ) and (ii) explore the atmospheric chemistry of temperate gas giants.

Acknowledgments

We thank the anonymous referee for valuable feedback that improved the quality of this manuscript. C.I.C. acknowledges support by NASA Headquarters through an appointment to the NASA Postdoctoral Program at the Goddard Space Flight Center, administered by USRA through a contract with NASA and the NASA Earth and Space Science Fellowship Program through grant 80NSSC18K1114. S.K. acknowledges research support from the Carnegie Institution of Science through the Carnegie Fellowship. G.S. acknowledges support provided by NASA through NASA Hubble Fellowship grant HST-HF2-51519.001-A awarded by STScI, which is operated by AURA for NASA under contract NAS5-26555. The Center for Exoplanets and Habitable Worlds is supported by the Pennsylvania State University and the Eberly College of Science.

The computations for this research were performed on Pennsylvania State University's Institute for Computational and Data Sciences' Roar supercomputer. This content is solely the responsibility of the authors and does not necessarily represent the views of the Institute for Computational and Data Sciences.

We acknowledge support from NSF grants AST 1006676, AST 1126413, AST 1310875, AST 1310885, AST 2009554, AST 2009889, AST 2108512, and AST 2108801 and the NASA Astrobiology Institute (NNA09DA76A) in our pursuit of precision RVs in the near-infrared. We acknowledge support from the Heising-Simons Foundation via grant 2017-0494.

Some of these results are based on observations obtained with the Apache Point Observatory 3.5 m telescope, which is owned and operated by the Astrophysical Research Consortium. We acknowledge support from NSF grants AST 1907622, AST 1909506, AST 1909682, and AST 1910954 and the Research Corporation in connection with precision diffuser-assisted photometry. We wish to thank the APO 3.5 m telescope operators for their assistance in obtaining these data.

These results are based on observations obtained with HPF and LRS2 on the HET. The HET is a joint project of the University of Texas at Austin, Pennsylvania State University, Ludwig-Maximilians-Universität München, and Georg-August Universität Gottingen. The HET is named in honor of its principal benefactors, William P. Hobby and Robert E. Eberly. The HET collaboration acknowledges the support and resources from the Texas Advanced Computing Center. We are grateful to the HET Resident Astronomers and Telescope Operators for their valuable assistance in gathering our HPF data. The LRS2 was developed and funded by the University of Texas at Austin McDonald Observatory and Department of Astronomy and by Pennsylvania State University. We thank the Leibniz-Institut für Astrophysik Potsdam (AIP) and the Institut für Astrophysik Göttingen (IAG) for their contributions to the construction of the integral field units. We would like to acknowledge that the HET is built on Indigenous land. Moreover, we would like to acknowledge and pay our respects to the Carrizo & Comecrudo, Coahuiltecan, Caddo, Tonkawa, Comanche, Lipan Apache, Alabama-Coushatta, Kickapoo, Tigua Pueblo, and all of the American Indian and Indigenous peoples and communities who have been or have become a part of these lands and territories on Turtle Island in Texas.

Some of the data were obtained by the NEID spectrograph built by Pennsylvania State University and operated at the WIYN Observatory by NOIRLab, which is managed by the Association of Universities for Research in Astronomy (AURA) under a cooperative agreement with the NSF and operated under the NN-EXPLORE partnership of NASA and the NSF. WIYN is a joint facility of the University of Wisconsin–Madison, Indiana University, NSF's NOIRLab, Pennsylvania State University, Purdue University, the University of California–Irvine, and the University of Missouri. Observations with NEID were obtained under proposal 2022A-763446 (PI: S. Wang). The NEID results utilize the Data Reduction Pipeline operated by NExScI and developed under subcontract 1644767 between JPL and the University of Arizona. This work was performed for the Jet Propulsion Laboratory, California Institute of Technology, sponsored by the United States Government under prime contract 80NM0018D0004 between Caltech and NASA. We thank the NEID Queue Observers and WIYN Observing Associates for their skillful execution of the NEID observations. We thank Zade Arnold, Joe Davis, Michelle Edwards, John Ehret, Tina Juan, Brian Pisarek, Aaron Rowe, Fred Wortman, the Eastern Area Incident Management Team, and all of the firefighters and air support crew who fought the recent Contreras fire to save KPNO. The authors are honored to be permitted to conduct astronomical research on Iolkam Du'ag (Kitt Peak), a mountain with particular significance to the Tohono O'odham.

Some of the observations in this paper made use of the NN-EXPLORE Exoplanet and Stellar Speckle Imager (NESSI). NESSI was funded by the NASA Exoplanet Exploration Program and the NASA Ames Research Center. NESSI was built at the Ames Research Center by Steve B. Howell, Nic Scott, Elliott P. Horch, and Emmett Quigley.

This paper is based on observations obtained from the Las Campanas Remote Observatory through a partnership between the Carnegie Observatories, the Astro-Physics Corporation, Howard Hedlund, Michael Long, Dave Jurasevich, and the SSC Observatories.

Some of the data presented in this paper were obtained from MAST at STScI. The specific observations analyzed can be accessed via DOI:10.17909/1xcp-2f18. Support for MAST for non-HST data is provided by the NASA Office of Space Science via grant NNX09AF08G and other grants and contracts. This work includes data collected by the TESS mission that are publicly available from MAST. Funding for the TESS mission is provided by the NASA Science Mission directorate. This research made use of (i) the NASA Exoplanet Archive, which is operated by Caltech, under contract with NASA under the Exoplanet Exploration Program; (ii) the SIMBAD database, operated at CDS, Strasbourg, France; (iii) NASA's Astrophysics Data System Bibliographic Services; (iv) the NASA/IPAC Infrared Science Archive, which is funded by NASA and operated by the California Institute of Technology; and (v) data from 2MASS, a joint project of the University of Massachusetts and IPAC at Caltech, funded by NASA and the NSF.

This work has made use of data from the European Space Agency (ESA) mission Gaia (https://www.cosmos.esa.int/gaia), processed by the Gaia Data Processing and Analysis Consortium (DPAC; https://www.cosmos.esa.int/web/gaia/

dpac/consortium). Funding for the DPAC has been provided by national institutions, in particular the institutions participating in the Gaia Multilateral Agreement.

Some of the observations in this paper made use of the Guoshoujing Telescope (LAMOST), a National Major Scientific Project built by the Chinese Academy of Sciences. Funding for the project has been provided by the National Development and Reform Commission. LAMOST is operated and managed by the National Astronomical Observatories, Chinese Academy of Sciences.

Some of the observations in this paper were obtained using the Samuel Oschin Telescope 48-inch and the 60-inch Telescope at the Palomar Observatory as part of the ZTF project. The ZTF is supported by the NSF under grant No. AST-2034437 and a collaboration including Caltech, IPAC, the Weizmann Institute for Science, the Oskar Klein Center at Stockholm University, the University of Maryland, Deutsches Elektronen-Synchrotron and Humboldt University, the TANGO Consortium of Taiwan, the University of Wisconsin at Milwaukee, Trinity College Dublin, Lawrence Livermore National Laboratories, and IN2P3, France. Operations are conducted by COO, IPAC, and UW.

Facilities: ARC (ARCTIC), Exoplanet Archive, Gaia, HET (HPF, LRS2), Las Campanas Observatory (TMMT, LCRO), LAMOST, MAST, PO:1.2 m (ZTF), PO:1.5 m (ZTF), TESS, WIYN (NESSI).

Software: `astroquery` (Ginsburg et al. 2019), `astropy` (Astropy Collaboration et al. 2018), `barycorrpy` (Kanodia & Wright 2018), `dynesty` (Speagle 2020), `eleanor` (Feinstein et al. 2019), `EXOFASTv2` (Eastman et al. 2019), `GLS` (Zechmeister & Kürster 2009), `HPF-SpecMatch`, `juliet` (Espinoza et al. 2019), `lightkurve` (Lightkurve Collaboration et al. 2018), `LRS2Multi`, `matplotlib` (Hunter 2007), `numpy` (van der Walt et al. 2011), `Panacea`, `pandas` (McKinney 2010), `PyHammer` (Roulston et al. 2020), `scipy` (Virtanen et al. 2020), `telfit` (Gullikson et al. 2014), `thejoker` (Price-Whelan et al. 2017), `TLS` (Hippke & Heller 2019), `WD_models` (Cheng et al. 2019).

Appendix A
SED Fit to Broadband Photometry

The SED fits with `EXOFASTv2` use Gaussian priors on (i) the broadband photometry listed in Table 3; (ii) the $\log g_\star$, T_e, and [Fe/H] derived from `HPF-SpecMatch`; and (iii) the geometric distance calculated from Bailer-Jones et al. (2021) for each respective star. We apply an upper limit to the visual extinction based on estimates of Galactic dust (Green et al. 2019) calculated at the distance determined by Bailer-Jones et al. (2021). The $R_v = 3.1$ reddening law from Fitzpatrick (1999) is used to convert the extinction from Green et al. (2019) to a visual magnitude extinction. The stellar parameters derived using the Gaia DR3 parallax are identical to the values derived with the Bailer-Jones et al. (2021) distance priors. This is expected because Bailer-Jones et al. (2021) noted that the inverse parallax provides a good distance estimate for stars with positive parallaxes and a ratio between the parallax error to the parallax of $\sigma_\varpi/\varpi < 0.1$. Figures 12 and 13 present the SED fits for TOI-3984 A and TOI-5293 A, respectively.

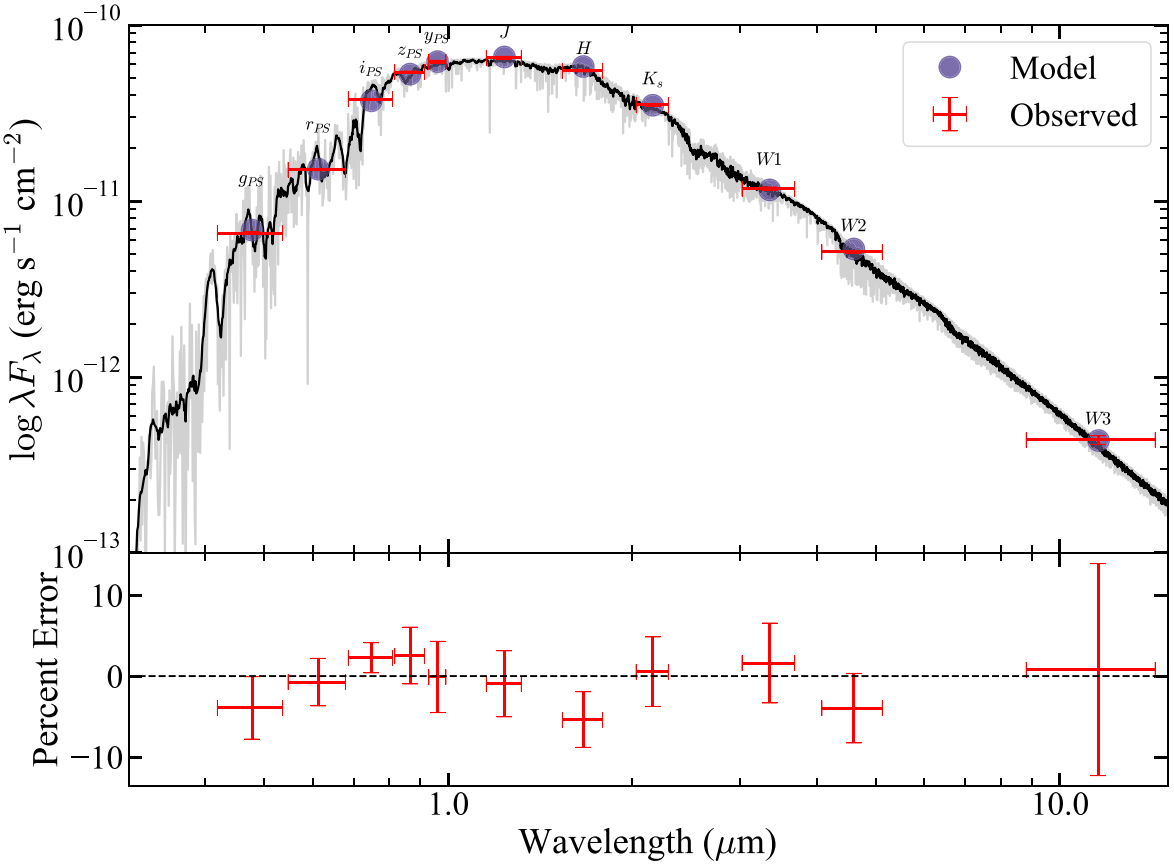

Figure 12. The SED fit to TOI-3984 A. Red points are the measurements from broadband photometry, while blue points represent the MIST model flux. The horizontal bars represent the width for each filter. A NextGen BT-SETTL model (Allard et al. 2012) is overlaid for reference as a gray line and smoothed for clarity as a black line. The BT-SETTL model is not used as part of the SED fit.

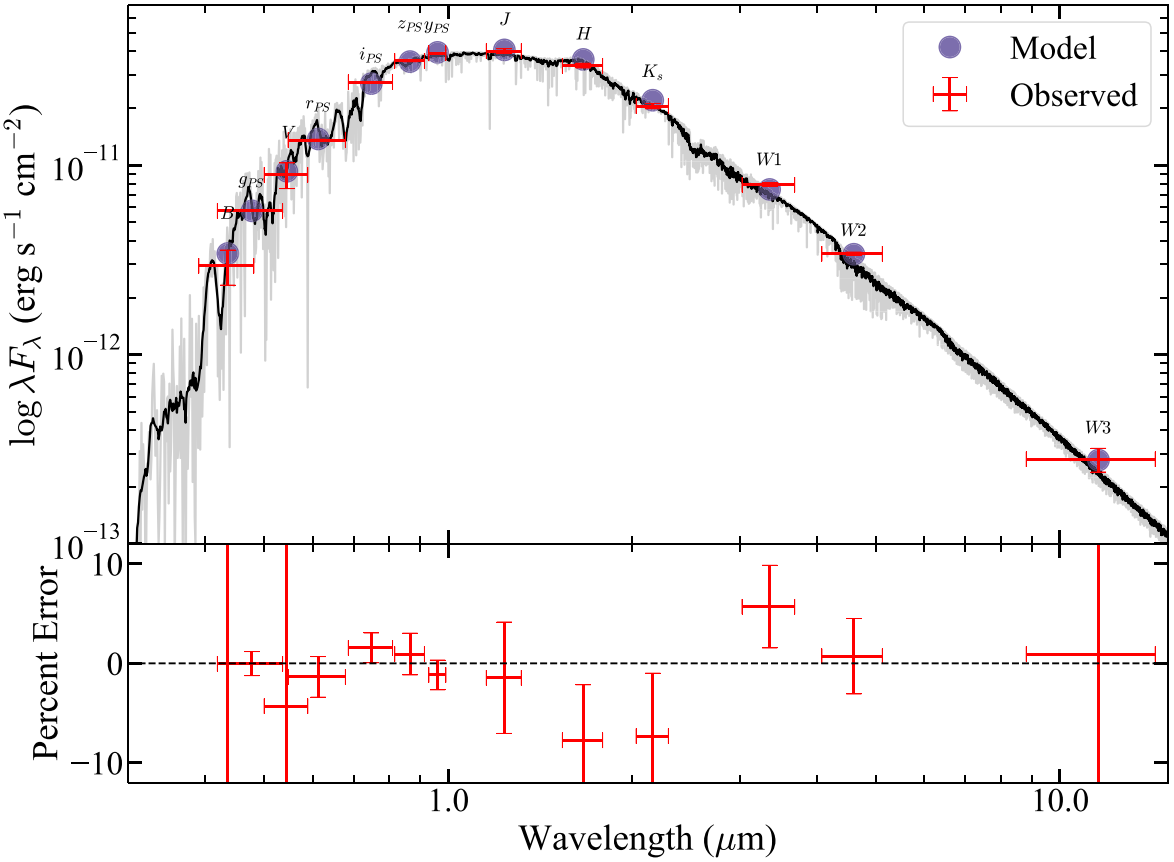

Figure 13. Same as Figure 12 but for TOI-5293 A.

Appendix B
Measuring the Rotation Period

B.1. TESS

We do not search for photometric modulation using the TESS PDCSAP flux or `eleanor` `CORR_FLUX` because the algorithms that produce these light curves are known to attenuate and distort long-period (>10 days) astrophysical signals such as starspot-induced photometric variability (see Gilliland et al. 2015; Van Cleve et al. 2016; Feinstein et al. 2019; Holcomb et al. 2022). We use the TESS Systematics-insensitive Periodogram package (`TESS-SIP`; Hedges et al. 2020) to simultaneously detrend systematics in the uncorrected flux and create a Lomb–Scargle periodogram. `TESS-SIP` uses a linear model consisting of regressors (for this search, three principal components and a mean offset) and a sinusoid component. We limit the search to periods between 1 and 60 days and analyze all available long-cadence data after excising the transits and bad-quality data (nonzero TESS quality flags) for each star. No significant periods for TOI-3984 A and TOI-5293 A were recovered.

B.2. ZTF

TOI-3984 A and TOI-5293 A were observed with ZTF as part of a survey of the TESS northern sectors (van Roestel et al. 2019), and the photometry is publicly available under DR15.[49] The ZTF has a plate scale of $1\farcs012\,\mathrm{pixel}^{-1}$ (Yao et al. 2019), and all exposures for these objects are 30 s. We use the constraints from the ZTF Science Data System Explanatory Supplement[50] (ZDS) and reject observations with (i) nonzero `catflag` values (see Section 13.6 in ZDS); (ii) values of $\chi < 0.5$ and >1.5, where χ is the rms of the residuals to the PSF fit on the source performed by the ZTF pipeline; (iii) values of $|\texttt{sharp}| \geqslant 0.5$, where `sharp` is the difference of the observed and model squared PSF FWHM; and (iv) airmass >1.8. TOI-3984 A has (i) 471 observations in the *zg* filter between 2018 March 25 and 2022 July 22 with a median cadence and precision of 1 day and ∼1.3% and (ii) 498 observations in the *zr* filter between 2018 March 21 and 2022 July 17 with a median cadence and precision of 1 day and ∼1.1%. TOI-5293 A has (i) 197 observations in the *zg* filter between 2018 June 26 and 2022 November 6 with a median cadence and precision of 3 days and ∼1.5% and (ii) 181 observations in the *zr* filter between 2018 June 29 and 2022 October 26 with a median cadence and precision of 3 days and ∼1.1%.

To derive the rotation period, we modeled the ZTF photometry with the `juliet` analysis package (Espinoza et al. 2019), which performs the parameter estimation using the dynamic nested-sampling algorithm `dynesty` (Speagle 2020). The photometric model consists of a Gaussian process noise model with the approximate quasiperiodic covariance function from Foreman-Mackey et al. (2017). This kernel has allowed for computationally efficient inference of stellar rotation periods in large data sets that are not uniformly sampled (e.g., Angus et al. 2018).

[49] https://www.ztf.caltech.edu/ztf-public-releases.html

[50] https://web.ipac.caltech.edu/staff/fmasci/ztf/ztf_pipelines_deliverables.pdf

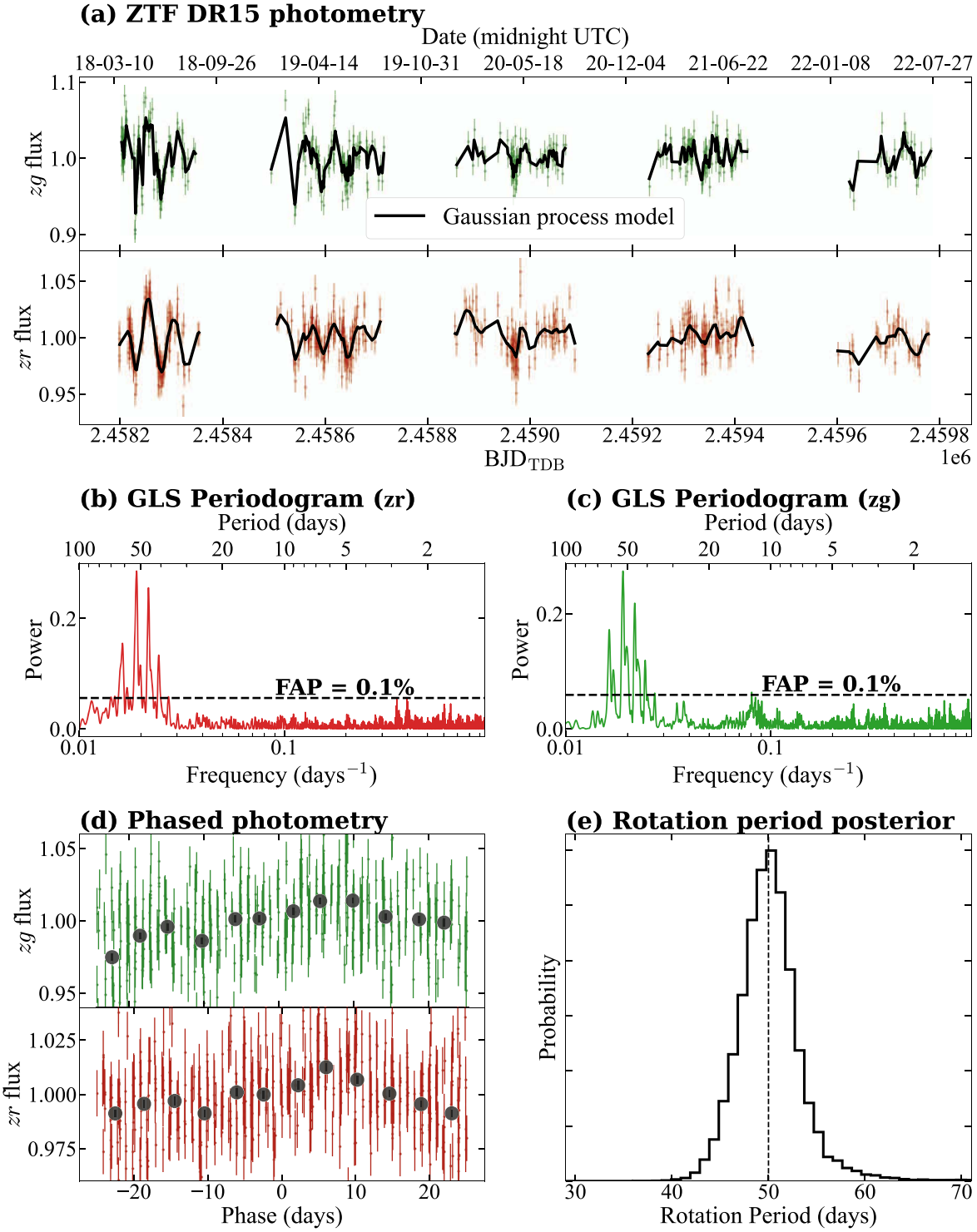

Figure 14. Panel (a) displays the ZTF photometry for TOI-3984 A in each filter along with the best-fitting Gaussian process model for reference. Panels (b) and (c) are the GLS periodograms for the *zr* and *zg* photometry from ZTF. An FAP of 0.01% (following Zechmeister & Kürster 2009) is shown for reference. Panel (d) presents the ground-based ZTF photometry from panel (a) phased to the derived rotation period. The large black points represent 4 day bins of the phased photometry. Panel (e) presents the posterior distribution of the rotation period from the Gaussian process model. The derived rotation period is $50.0^{+2.8}_{-2.7}$ days.

We interpret the periodicity of the Gaussian process kernel as the stellar rotation period and force the same kernel periodicity for both ZTF filters of the same star. We include a simple white-noise model $\sigma_{\rm phot}$ in the form of a jitter term that is added in quadrature to the error bars of the photometry for each filter. The fit for each star uses a uniform prior on the Gaussian process period of 1.1–100 days, where the upper limit reflects the upper limits from other photometric surveys of mid-M dwarfs (McQuillan et al. 2013; Newton et al. 2018). The priors and posterior values for the fits to the ZTF photometry are listed in Table 6. The ZTF data and best-fitting Gaussian process models are presented in Figure 14 and 15 for TOI-3984 A and TOI-5293 A, respectively.

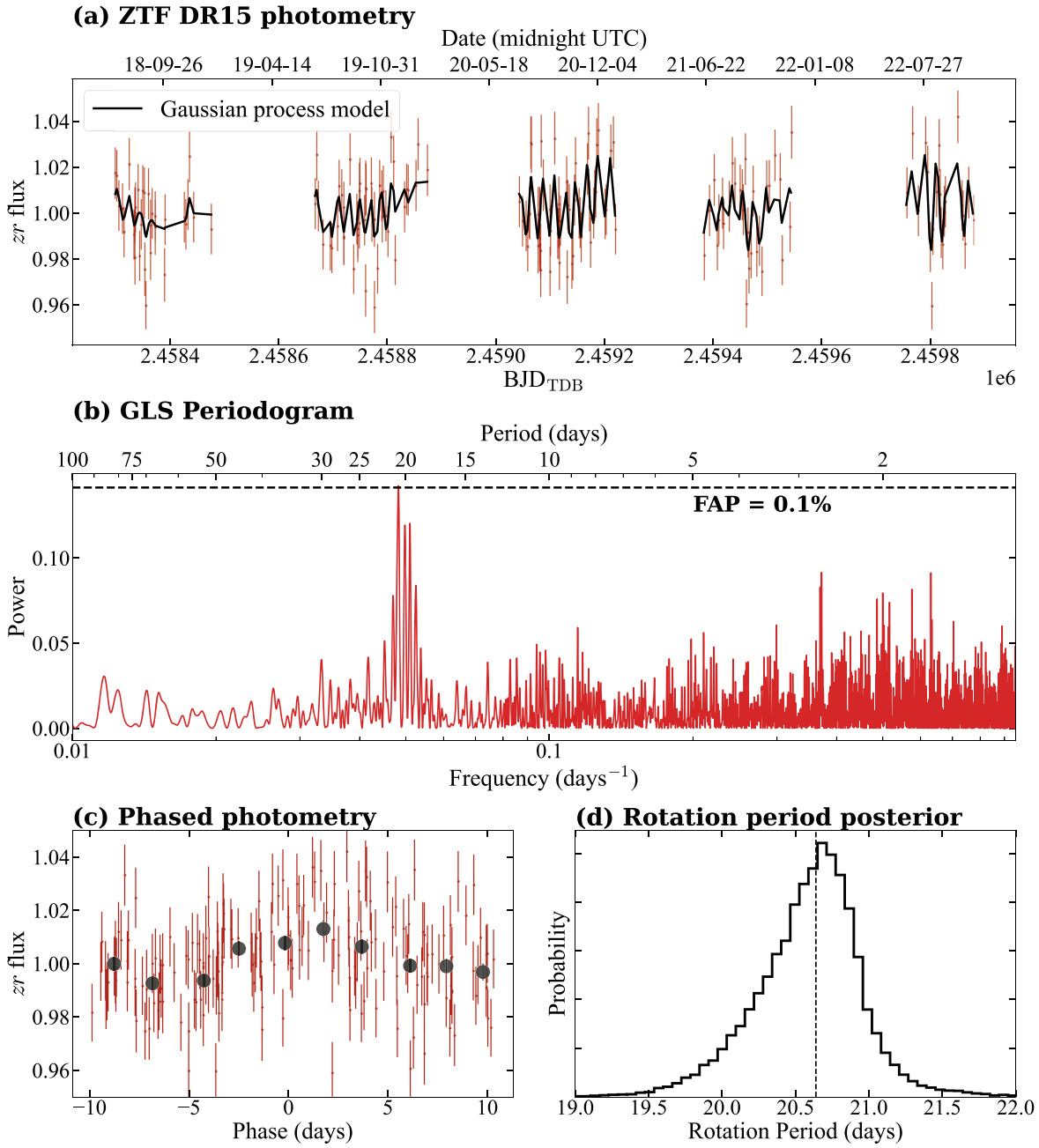

Figure 15. Same as Figure 14 but for TOI-5293 A. Panel (a) displays the ZTF photometry along with the best-fitting Gaussian process model for reference. Panel (b) presents the GLS periodogram for the ZTF data. Panel (c) presents the phased ground-based ZTF photometry, with large black points representing 2 day bins. Panel (d) presents the posterior distribution of the rotation period. The derived rotation period is $20.6^{+0.3}_{-0.4}$ days.

Table 6
ZTF Photometric Modeling

Parameter	Units	Prior	TOI-3984 A	TOI-5293 A
zg Gaussian Process Parameters				
B	Amplitude (ppm)	$\mathcal{J}(10^{-4}, 10^{12})$	470^{+70}_{-60}	...
C	Additive factor	$\mathcal{J}(10^{-3}, 10^{3})$	$0.8^{+100}_{-0.8}$	...
L	Length scale (days)	$\mathcal{J}(10^{-3}, 10^{3})$	$4.6^{+1.2}_{-0.9}$	...
Photometric jitter	$\sigma_{\rm phot}$ (ppm)	$\mathcal{J}(10^{-6}, 10^{3})$	$0.03^{+45.07}_{-0.03}$	...
zr Gaussian Process Parameters				
B	Amplitude (ppm)	$\mathcal{J}(10^{-4}, 10^{12})$	200^{+60}_{-40}	160^{+60}_{-50}
C	Additive factor	$\mathcal{J}(10^{-3}, 10^{3})$	$0.02^{+0.21}_{-0.02}$	$0.03^{+0.3}_{-0.02}$
L	Length scale (days)	$\mathcal{J}(10^{-3}, 10^{3})$	60^{+40}_{-20}	120^{+200}_{-70}
Photometric jitter	$\sigma_{\rm phot}$ (ppm)	$\mathcal{J}(10^{-6}, 10^{3})$	$0.03^{+43.36}_{-0.03}$	$0.05^{+42.17}_{-0.05}$
Shared Gaussian Process Parameters				
$P_{\rm GP}$	Period (days)	$\mathcal{J}(1.1, 100)$	$50.0^{+2.8}_{-2.7}$	$20.6^{+0.3}_{-0.4}$

Appendix C
White Dwarf Companion to TOI-3984 A

We use the nominal Gaia DR3 colors to predict the mass and cooling age using the `WD_models` package and the models from Bédard et al. (2020) for a hydrogen-dominated atmosphere. Figure 16 displays the location of TOI-3984 B (TIC 1101522311) on the Gaia color–magnitude diagram (data from Gentile Fusillo et al. 2021) along with the best-matching model used to derive a photometric age and mass from its location.

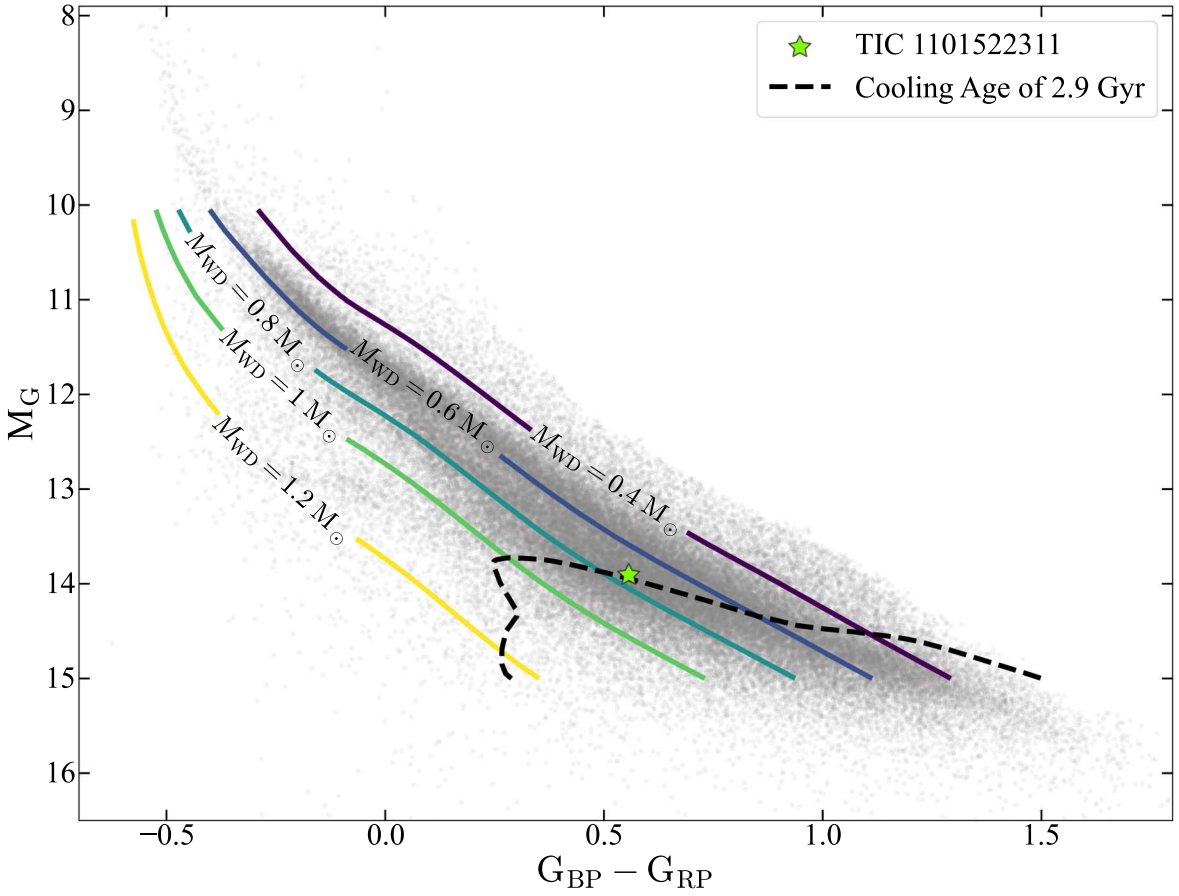

Figure 16. Nominal position of TIC 1101522311, the white dwarf companion to TOI-3984 A, on the color–magnitude diagram for white dwarfs identified in Gaia EDR3 by Gentile Fusillo et al. (2021). Contours for fixed masses from Bédard et al. (2020) are plotted for reference. The best-matching cooling track from the models is shown with a dashed line.

ORCID iDs

Caleb I. Cañas https://orcid.org/0000-0003-4835-0619
Shubham Kanodia https://orcid.org/0000-0001-8401-4300
Jessica Libby-Roberts https://orcid.org/0000-0002-2990-7613
Andrea S. J. Lin https://orcid.org/0000-0002-9082-6337
Maria Schutte https://orcid.org/0000-0003-2435-130X
Luke Powers https://orcid.org/0000-0002-5300-5353
Sinclaire Jones https://orcid.org/0000-0002-7227-2334
Andrew Monson https://orcid.org/0000-0002-0048-2586
Songhu Wang https://orcid.org/0000-0002-7846-6981
Guðmundur Stefánsson https://orcid.org/0000-0001-7409-5688
William D. Cochran https://orcid.org/0000-0001-9662-3496
Paul Robertson https://orcid.org/0000-0003-0149-9678
Suvrath Mahadevan https://orcid.org/0000-0001-9596-7983
Adam F. Kowalski https://orcid.org/0000-0001-7458-1176
John Wisniewski https://orcid.org/0000-0001-9209-1808
Brock A. Parker https://orcid.org/0000-0001-9307-8170
Alexander Larsen https://orcid.org/0000-0002-2401-8411
Henry A. Kobulnicky https://orcid.org/0000-0002-4475-4176
Arvind F. Gupta https://orcid.org/0000-0002-5463-9980
Mark E. Everett https://orcid.org/0000-0002-0885-7215
Bryan Edward Penprase https://orcid.org/0000-0002-7000-3181
Gregory Zeimann https://orcid.org/0000-0003-2307-0629
Corey Beard https://orcid.org/0000-0001-7708-2364
Chad F. Bender https://orcid.org/0000-0003-4384-7220
Knicole D. Colón https://orcid.org/0000-0001-8020-7121
Scott A. Diddams https://orcid.org/0000-0002-2144-0764
Connor Fredrick https://orcid.org/0000-0002-0560-1433
Samuel Halverson https://orcid.org/0000-0003-1312-9391
Joe P. Ninan https://orcid.org/0000-0001-8720-5612
Lawrence W. Ramsey https://orcid.org/0000-0002-4289-7958
Arpita Roy https://orcid.org/0000-0001-8127-5775
Christian Schwab https://orcid.org/0000-0002-4046-987X

References

Addison, B. C., Horner, J., Wittenmyer, R. A., et al. 2021, AJ, 162, 137
Akaike, H. 1974, ITAC, 19, 716
Akeson, R. L., Chen, X., Ciardi, D., et al. 2013, PASP, 125, 989
Albrecht, S., Winn, J. N., Johnson, J. A., et al. 2012, ApJ, 757, 18
Albrecht, S. H., Dawson, R. I., & Winn, J. N. 2022, PASP, 134, 082001
Albrecht, S. H., Marcussen, M. L., Winn, J. N., Dawson, R. I., & Knudstrup, E. 2021, ApJL, 916, L1
Allard, F., Homeier, D., & Freytag, B. 2012, RSPTA, 370, 2765
Alonso, R. 2018, in Handbook of Exoplanets, ed. H. J. Deeg & J. A. Belmonte (Berlin: Springer), 40
Anderson, K. R., Lai, D., & Pu, B. 2020, MNRAS, 491, 1369
Andrae, R., Fouesneau, M., Sordo, R., et al. 2022, arXiv:2206.06138
Andrews, S. M., Rosenfeld, K. A., Kraus, A. L., & Wilner, D. J. 2013, ApJ, 771, 129
Anglada-Escudé, G., & Butler, R. P. 2012, ApJS, 200, 15
Angus, R., Morton, T., Aigrain, S., Foreman-Mackey, D., & Rajpaul, V. 2018, MNRAS, 474, 2094
Ansdell, M., Williams, J. P., Manara, C. F., et al. 2017, AJ, 153, 240
Astropy Collaboration, Price-Whelan, A. M., Sipőcz, B. M., et al. 2018, AJ, 156, 123
Bailer-Jones, C. A. L., Rybizki, J., Fouesneau, M., Demleitner, M., & Andrae, R. 2021, AJ, 161, 147
Baraffe, I., Chabrier, G., & Barman, T. 2008, A&A, 482, 315
Baruteau, C., Crida, A., Paardekooper, S. J., et al. 2014, in Protostars and Planets VI, ed. H. Beuther et al. (Tucson, AZ: Univ. Arizona Press), 667
Batalha, N. E., Lewis, T., Fortney, J. J., et al. 2019, ApJL, 885, L25
Batygin, K., Bodenheimer, P. H., & Laughlin, G. P. 2016, ApJ, 829, 114
Bakos, G. Á., Bayliss, D., Bento, J., et al. 2020, AJ, 159, 267
Becker, J. C., Vanderburg, A., Adams, F. C., Rappaport, S. A., & Schwengeler, H. M. 2015, ApJL, 812, L18
Bédard, A., Bergeron, P., Brassard, P., & Fontaine, G. 2020, ApJ, 901, 93
Beleznay, M., & Kunimoto, M. 2022, MNRAS, 516, 75
Bellm, E. C., Kulkarni, S. R., Graham, M. J., et al. 2019, PASP, 131, 018002
Belokurov, V., Penoyre, Z., Oh, S., et al. 2020, MNRAS, 496, 1922
Bensby, T., Feltzing, S., & Lundström, I. 2003, A&A, 410, 527
Bessell, M. S. 1990, PASP, 102, 1181
Boley, A. C., Granados Contreras, A. P., & Gladman, B. 2016, ApJL, 817, L17
Bonfils, X., Delfosse, X., Udry, S., et al. 2013, A&A, 549, A109
Bonomo, A. S., Desidera, S., Benatti, S., et al. 2017, A&A, 602, A107
Boss, A. P. 1997, Sci, 276, 1836
Bourrier, V., Lovis, C., Beust, H., et al. 2018, Natur, 553, 477
Bourrier, V., Zapatero Osorio, M. R., Allart, R., et al. 2022, A&A, 663, A160
Bovy, J. 2015, ApJS, 216, 29
Brady, M., Bean, J. L., Seifahrt, A., et al. 2023, AJ, 165, 129
Bryant, E. M., Bayliss, D., & Van Eylen, V. 2023, MNRAS, 521, 3663
Burn, R., Schlecker, M., Mordasini, C., et al. 2021, A&A, 656, A72
Burrows, A., & Sharp, C. M. 1999, ApJ, 512, 843
Burt, J. A., Nielsen, L. D., Quinn, S. N., et al. 2020, AJ, 160, 153
Cañas, C. I., Kanodia, S., Bender, C. F., et al. 2022, AJ, 164, 50
Cañas, C. I., Wang, S., Mahadevan, S., et al. 2019, ApJ, 870, L17
Chabrier, G., Johansen, A., Janson, M., & Rafikov, R. 2014, in Protostars and Planets VI, ed. H. Beuther et al. (Tucson, AZ: Univ. Arizona Press), 619
Chambers, K. C., Magnier, E. A., Metcalfe, N., et al. 2016, arXiv:1612.05560
Cheng, S., Cummings, J. D., & Ménard, B. 2019, ApJ, 886, 100
Choi, J., Dotter, A., Conroy, C., et al. 2016, ApJ, 823, 102
Chonis, T. S., Hill, G. J., Lee, H., et al. 2016, Proc. SPIE, 9908, 99084C
Chonis, T. S., Hill, G. J., Lee, H., Tuttle, S. E., & Vattiat, B. L. 2014, Proc. SPIE, 9147, 91470A
Collins, K. A., Kielkopf, J. F., Stassun, K. G., & Hessman, F. V. 2017, AJ, 153, 77
Creevey, O. L., & Lebreton, Y. 2022, Masses and Ages from FLAME in DR3, Technical Note, Observatoire de la Cote d'Azur, Nice, https://dms.cosmos.esa.int/COSMOS/doc_fetch.php?id=1612899
Creevey, O. L., Sordo, R., Pailler, F., et al. 2022, arXiv:2206.05864
Cui, X.-Q., Zhao, Y.-H., Chu, Y.-Q., et al. 2012, RAA, 12, 1197
Cumming, A., Butler, R. P., Marcy, G. W., et al. 2008, PASP, 120, 531
Cummings, J. D., Kalirai, J. S., Tremblay, P. E., Ramirez-Ruiz, E., & Choi, J. 2018, ApJ, 866, 21
Cutri, R. M., Skrutskie, M. F., van Dyk, S., et al. 2003, yCat, II/246
Dash, S., Majumdar, L., Willacy, K., et al. 2022, ApJ, 932, 20
Dawson, R. I., & Johnson, J. A. 2018, ARA&A, 56, 175
Deng, L.-C., Newberg, H. J., Liu, C., et al. 2012, RAA, 12, 735
Dotter, A. 2016, ApJS, 222, 8
Dressing, C. D., & Charbonneau, D. 2015, ApJ, 807, 45
Durisen, R. H., Boss, A. P., Mayer, L., et al. 2007, in Protostars and Planets V, ed. B. Reipurth, D. Jewitt, & K. Keil (Tucson, AZ: Univ. Arizona Press), 607
Eastman, J. D., Rodriguez, J. E., Agol, E., et al. 2019, arXiv:1907.09480
El-Badry, K., & Rix, H.-W. 2018, MNRAS, 480, 4884
El-Badry, K., Rix, H.-W., & Heintz, T. M. 2021, MNRAS, 506, 2269
Endl, M., Cochran, W. D., Kürster, M., et al. 2006, ApJ, 649, 436
Engle, S. G., & Guinan, E. F. 2018, RNAAS, 2, 34
Espinoza, N., Kossakowski, D., & Brahm, R. 2019, MNRAS, 490, 2262
Evans, D. F., Southworth, J., Smalley, B., et al. 2018a, A&A, 610, A20
Evans, D. W., Riello, M., De Angeli, F., et al. 2018b, A&A, 616, A4
Fabrycky, D., & Tremaine, S. 2007, ApJ, 669, 1298
Feinstein, A. D., Montet, B. T., Foreman-Mackey, D., et al. 2019, PASP, 131, 094502
Fitzpatrick, E. L. 1999, PASP, 111, 63
Fontanive, C., & Bardalez Gagliuffi, D. 2021, FrASS, 8, 16
Fontanive, C., Rice, K., Bonavita, M., et al. 2019, MNRAS, 485, 4967
Ford, E. B., & Rasio, F. A. 2008, ApJ, 686, 621
Foreman-Mackey, D., Agol, E., Ambikasaran, S., & Angus, R. 2017, AJ, 154, 220
Fortney, J. J., Dawson, R. I., & Komacek, T. D. 2021, JGRE, 126, e06629
Fortney, J. J., Marley, M. S., & Barnes, J. W. 2007, ApJ, 659, 1661
Fortney, J. J., Visscher, C., Marley, M. S., et al. 2020, AJ, 160, 288
Frazier, R. C., Stefánsson, G., Mahadevan, S., et al. 2023, ApJL, 944, L41
Fulton, B. J., Petigura, E. A., Blunt, S., & Sinukoff, E. 2018, PASP, 130, 044504
Gagné, J., Mamajek, E. E., Malo, L., et al. 2018, ApJ, 856, 23

Gaia Collaboration, Vallenari, A., Brown, A. G. A., et al. 2022, A&A, 674, A1
Gallet, F., Bolmont, E., Mathis, S., Charbonnel, C., & Amard, L. 2017, A&A, 604, A112
Gan, T., Wang, S. X., Wang, S., et al. 2023, AJ, 165, 17
Gao, P., Wakeford, H. R., Moran, S. E., & Parmentier, V. 2021, JGRE, 126, e06655
Gentile Fusillo, N. P., Tremblay, P. E., Cukanovaite, E., et al. 2021, MNRAS, 508, 3877
Gibson, S. R., Howard, A. W., Marcy, G. W., et al. 2016, Proc. SPIE, 9908, 990870
Gilliland, R. L., Chaplin, W. J., Jenkins, J. M., Ramsey, L. W., & Smith, J. C. 2015, AJ, 150, 133
Ginsburg, A., Sipőcz, B. M., Brasseur, C. E., et al. 2019, AJ, 157, 98
Goldreich, P., & Tremaine, S. 1980, ApJ, 241, 425
Graham, M. J., Kulkarni, S. R., Bellm, E. C., et al. 2019, PASP, 131, 078001
Gray, D. F. 2008, The Observation and Analysis of Stellar Photospheres (Cambridge: Cambridge Univ. Press)
Green, G. M., Schlafly, E., Zucker, C., Speagle, J. S., & Finkbeiner, D. 2019, ApJ, 887, 93
Greene, T. P., Line, M. R., Montero, C., et al. 2016, ApJ, 817, 17
Gullikson, K., Dodson-Robinson, S., & Kraus, A. 2014, AJ, 148, 53
Halverson, S., Terrien, R., Mahadevan, S., et al. 2016, Proc. SPIE, 9908, 99086P
Hardegree-Ullman, K. K., Cushing, M. C., Muirhead, P. S., & Christiansen, J. L. 2019, AJ, 158, 75
Hayward, T. L., Brandl, B., Pirger, B., et al. 2001, PASP, 113, 105
Hedges, C., Angus, R., Barentsen, G., et al. 2020, RNAAS, 4, 220
Helling, C., Woitke, P., & Thi, W. F. 2008, A&A, 485, 547
Henden, A. A., Levine, S., Terrell, D., et al. 2018, AAS Meeting Abstracts, 232, 223.06
Hill, G. J., Lee, H., MacQueen, P. J., et al. 2021, AJ, 162, 298
Hippke, M., & Heller, R. 2019, A&A, 623, A39
Hirano, T., Gaidos, E., Winn, J. N., et al. 2020a, ApJL, 890, L27
Hirano, T., Krishnamurthy, V., Gaidos, E., et al. 2020b, ApJL, 899, L13
Hobbs, R., Shorttle, O., & Madhusudhan, N. 2022, MNRAS, 516, 1032
Holcomb, R. J., Robertson, P., Hartigan, P., Oelkers, R. J., & Robinson, C. 2022, ApJ, 936, 138
Hord, B. J., Colón, K. D., Berger, T. A., et al. 2022, AJ, 164, 13
Hord, B. J., Colón, K. D., Kostov, V., et al. 2021, AJ, 162, 263
Howard, A. W., Marcy, G. W., Bryson, S. T., et al. 2012, ApJS, 201, 15
Howell, S. B., Everett, M. E., Sherry, W., Horch, E., & Ciardi, D. R. 2011, AJ, 142, 19
Hsu, D. C., Ford, E. B., & Terrien, R. 2020, MNRAS, 498, 2249
Huang, C., Wu, Y., & Triaud, A. H. M. J. 2016, ApJ, 825, 98
Huang, C. X., Quinn, S. N., Vanderburg, A., et al. 2020c, ApJL, 892, L7
Huang, C. X., Vanderburg, A., Pál, A., et al. 2020a, RNAAS, 4, 204
Huang, C. X., Vanderburg, A., Pál, A., et al. 2020b, RNAAS, 4, 206
Huehnerhoff, J, Ketzeback, W., Bradley, A., et al. 2016, Proc. SPIE, 9908, 99085H
Hunter, J. D. 2007, CSE, 9, 90
Hwang, H.-C., Hamer, J. H., Zakamska, N. L., & Schlaufman, K. C. 2020, MNRAS, 497, 2250
Hwang, H.-C., Ting, Y.-S., & Zakamska, N. L. 2022, MNRAS, 512, 3383
Ida, S., & Lin, D. N. C. 2005, ApJ, 626, 1045
Ida, S., & Lin, D. N. C. 2008, ApJ, 673, 487
Jackson, B., Greenberg, R., & Barnes, R. 2008, ApJ, 678, 1396
Jenkins, J. M., Caldwell, D. A., Chandrasekaran, H., et al. 2010, ApJL, 713, L87
Jenkins, J. M., Twicken, J. D., McCauliff, S., et al. 2016, Proc. SPIE, 9913, 99133E
Johnson, D. R. H., & Soderblom, D. R. 1987, AJ, 93, 864
Jordán, A., Hartman, J. D., Bayliss, D., et al. 2022, AJ, 163, 125
Kanodia, S., Mahadevan, S., Libby-Roberts, J., et al. 2023, AJ, 165, 120
Kanodia, S., Mahadevan, S., Ramsey, L. W., et al. 2018, Proc. SPIE, 10702, 107026Q
Kanodia, S., & Wright, J. 2018, RNAAS, 2, 4
Kaplan, K. F., Bender, C. F., Terrien, R. C., et al. 2019, in ASP Conf. Ser. 523, Astronomical Data Analysis Software and Systems XXVII, ed. P. J. Teuben et al. (San Francisco, CA: ASP), 567
Kasper, D. H., Ellis, T. G., Yeigh, R. R., et al. 2016, PASP, 128, 105005
Kawashima, Y., Hu, R., & Ikoma, M. 2019, ApJL, 876, L5
Kempton, E. M. R., Bean, J. L., Louie, D. R., et al. 2018, PASP, 130, 114401
Kennedy, G. M., & Kenyon, S. J. 2008, ApJ, 673, 502
Kepler, S. O., Koester, D., Pelisoli, I., Romero, A. D., & Ourique, G. 2021, MNRAS, 507, 4646
Kesseli, A. Y., West, A. A., Veyette, M., et al. 2017, ApJS, 230, 16
Kilic, M., Bergeron, P., Kosakowski, A., et al. 2020, ApJ, 898, 84
Kipping, D. M. 2013a, MNRAS, 435, 2152
Kipping, D. M. 2013b, MNRAS, 434, L51
Kiseleva, L. G., Eggleton, P. P., & Mikkola, S. 1998, MNRAS, 300, 292
Knutson, H. A., Fulton, B. J., Montet, B. T., et al. 2014, ApJ, 785, 126
Kovács, G., Hodgkin, S., Sipőcz, B., et al. 2013, European Physical Journal Web of Conferences, 47, 01002
Kozai, Y. 1962, AJ, 67, 591
Kraus, A. L., Ireland, M. J., Huber, D., Mann, A. W., & Dupuy, T. J. 2016, AJ, 152, 8
Kreidberg, L. 2015, batman: BAsic Transit Model cAlculatioN in Python, Astrophysics Source Code Library, ascl:1510.002
Kunimoto, M., Daylan, T., Guerrero, N., et al. 2022, ApJS, 259, 33
Laughlin, G., Bodenheimer, P., & Adams, F. C. 2004, ApJL, 612, L73
Lépine, S., Rich, R. M., & Shara, M. M. 2007, ApJ, 669, 1235
Liang, M.-C., Seager, S., Parkinson, C. D., Lee, A. Y. T., & Yung, Y. L. 2004, ApJL, 605, L61
Liddle, A. R. 2007, MNRAS, 377, L74
Lidov, M. L. 1962, P&SS, 9, 719
Lightkurve Collaboration, Cardoso, J. V. d. M. a., Hedges, C., et al. 2018, Lightkurve: Kepler and TESS Time Series Analysis in Python, Astrophysics Source Code Library, ascl:1812.013
Lin, D. N. C., Bodenheimer, P., & Richardson, D. C. 1996, Natur, 380, 606
Lin, D. N. C., & Papaloizou, J. 1986, ApJ, 309, 846
Line, M. R., Liang, M. C., & Yung, Y. L. 2010, ApJ, 717, 496
Maciejewski, G. 2020, AcA, 70, 181
Madhusudhan, N. 2012, ApJ, 758, 36
Madhusudhan, N. 2016, ApJ, 827, 8
Madhusudhan, N. 2019, ARA&A, 57, 617
Madhusudhan, N., Mousis, O., Johnson, T. V., & Lunine, J. I. 2011, ApJ, 743, 191
Magnier, E. A., Schlafly, E. F., Finkbeiner, D. P., et al. 2020, ApJS, 251, 6
Mahadevan, S., Ramsey, L., Bender, C., et al. 2012, Proc. SPIE, 8446, 84461S
Mahadevan, S., Ramsey, L. W., Terrien, R., et al. 2014, Proc. SPIE, 9147, 91471G
Mai, C., & Line, M. R. 2019, ApJ, 883, 144
Manara, C. F., Morbidelli, A., & Guillot, T. 2018, A&A, 618, L3
Marley, M. S., Ackerman, A. S., Cuzzi, J. N., & Kitzmann, D. 2013, in Clouds and Hazes in Exoplanet Atmospheres, ed. S. J. Mackwell et al. (Tucson, AZ: Univ. Arizona Press), 367
Marley, M. S., & Robinson, T. D. 2015, ARA&A, 53, 279
Marzari, F., & Thebault, P. 2019, Galax, 7, 84
Masci, F. J., Laher, R. R., Rusholme, B., et al. 2019, PASP, 131, 018003
Mayor, M., Marmier, M., Lovis, C., et al. 2011, arXiv:1109.2497
McKinney, W. 2010, in Proc. 9th Python in Science Conf., ed. S. van der Walt & J. Millman (Austin, TX: SciPy), 51
McQuillan, A., Aigrain, S., & Mazeh, T. 2013, MNRAS, 432, 1203
Melbourne, K., Youngblood, A., France, K., et al. 2020, AJ, 160, 269
Metcalf, A., Anderson, T., Bender, C., et al. 2019, Optic, 6, 233
Millholland, S., Petigura, E., & Batygin, K. 2020, ApJ, 897, 7
Moe, M., & Kratter, K. M. 2021, MNRAS, 507, 3593
Mohanty, S., Greaves, J., Mortlock, D., et al. 2013, ApJ, 773, 168
Mollière, P., Molyarova, T., Bitsch, B., et al. 2022, ApJ, 934, 74
Mollière, P., van Boekel, R., Dullemond, C., Henning, T., & Mordasini, C. 2015, ApJ, 813, 47
Monson, A. J., Beaton, R. L., Scowcroft, V., et al. 2017, AJ, 153, 96
Moses, J. I., Visscher, C., Fortney, J. J., et al. 2011, ApJ, 737, 15
Mulders, G. D., Pascucci, I., & Apai, D. 2015, ApJ, 798, 112
Mustill, A. J., Davies, M. B., & Johansen, A. 2015, ApJ, 808, 14
Naoz, S. 2016, ARA&A, 54, 441
Newton, E. R., Irwin, J., Charbonneau, D., et al. 2016, ApJ, 821, 93
Newton, E. R., Mondrik, N., Irwin, J., Winters, J. G., & Charbonneau, D. 2018, AJ, 156, 217
Ngo, H., Knutson, H. A., Hinkley, S., et al. 2015, ApJ, 800, 138
Ninan, J. P., Bender, C. F., Mahadevan, S., et al. 2018, Proc. SPIE, 10709, 107092U
Nordhaus, J., & Spiegel, D. S. 2013, MNRAS, 432, 500
Nordhaus, J., Spiegel, D. S., Ibgui, L., Goodman, J., & Burrows, A. 2010, MNRAS, 408, 631
Öberg, K. I., Murray-Clay, R., & Bergin, E. A. 2011, ApJL, 743, L16
Öberg, K. I., & Wordsworth, R. 2019, AJ, 158, 194
Obermeier, C., Koppenhoefer, J., Saglia, R. P., et al. 2016, A&A, 587, A49
Palle, E., Oshagh, M., Casasayas-Barris, N., et al. 2020, A&A, 643, A25
Perri, F., & Cameron, A. G. W. 1974, Icar, 22, 416
Petigura, E. A., Marcy, G. W., Winn, J. N., et al. 2018, AJ, 155, 89
Petrovich, C. 2015a, ApJ, 805, 75

Petrovich, C. 2015b, ApJ, 799, 27
Pinamonti, M., Sozzetti, A., Maldonado, J., et al. 2022, A&A, 664, A65
Pineda, J. S., Youngblood, A., & France, K. 2021, ApJ, 911, 111
Pinhas, A., Madhusudhan, N., Gandhi, S., & MacDonald, R. 2019, MNRAS, 482, 1485
Pollack, J. B., Hubickyj, O., Bodenheimer, P., et al. 1996, Icar, 124, 62
Poon, S. T. S., Nelson, R. P., & Coleman, G. A. L. 2021, MNRAS, 505, 2500
Price-Whelan, A. M., Hogg, D. W., Foreman-Mackey, D., & Rix, H.-W. 2017, ApJ, 837, 20
Ramsey, L. W., Adams, M. T., Barnes, T. G., et al. 1998, Proc. SPIE, 3352, 34
Rasio, F. A., & Ford, E. B. 1996, Sci, 274, 954
Rice, M., Wang, S., & Laughlin, G. 2022, ApJL, 926, L17
Ricker, G. R., Winn, J. N., Vanderspek, R., et al. 2015, JATIS, 1, 014003
Riello, M., De Angeli, F., Evans, D. W., et al. 2021, A&A, 649, A3
Robertson, P., Anderson, T., Stefansson, G., et al. 2019, JATIS, 5, 015003
Roulston, B. R., Green, P. J., & Kesseli, A. Y. 2020, ApJS, 249, 34
Sabotta, S., Schlecker, M., Chaturvedi, P., et al. 2021, A&A, 653, A114
Schönrich, R., Binney, J., & Dehnen, W. 2010, MNRAS, 403, 1829
Schwab, C., Rakich, A., Gong, Q., et al. 2016, Proc. SPIE, 9908, 99087H
Schwarz, G. 1978, AnSta, 6, 461
Scott, N. J., Howell, S. B., Horch, E. P., & Everett, M. E. 2018, PASP, 130, 054502
Seifahrt, A., Bean, J. L., Stürmer, J., et al. 2016, Proc. SPIE, 9908, 990818
Sha, L., Vanderburg, A. M., Huang, C. X., et al. 2023, MNRAS, Advance Access
Shetrone, M., Cornell, M. E., Fowler, J. R., et al. 2007, PASP, 119, 556
Sing, D. K. 2018, arXiv:1804.07357
Sing, D. K., Fortney, J. J., Nikolov, N., et al. 2016, Natur, 529, 59
Smith, J. C., Stumpe, M. C., Van Cleve, J. E., et al. 2012, PASP, 124, 1000
Spalding, C., & Winn, J. N. 2022, ApJ, 927, 22
Speagle, J. S. 2020, MNRAS, 493, 3132
Stamatellos, D., & Herczeg, G. J. 2015, MNRAS, 449, 3432
Stassun, K. G., Oelkers, R. J., Paegert, M., et al. 2019, AJ, 158, 138
Stefánsson, G., Cañas, C., Wisniewski, J., et al. 2020a, AJ, 159, 100
Stefánsson, G., Hearty, F., Robertson, P., et al. 2016, ApJ, 833, 175
Stefánsson, G., Mahadevan, S., Hebb, L., et al. 2017, ApJ, 848, 9
Stefánsson, G., Mahadevan, S., Maney, M., et al. 2020b, AJ, 160, 192
Stefánsson, G., Mahadevan, S., Petrovich, C., et al. 2022, ApJL, 931, L15
Steffen, J. H., Ragozzine, D., Fabrycky, D. C., et al. 2012, PNAS, 109, 7982
Stumpe, M. C., Smith, J. C., Van Cleve, J. E., et al. 2012, PASP, 124, 985
Sudarsky, D., Burrows, A., & Hubeny, I. 2003, ApJ, 588, 1121
Tenenbaum, P., & Jenkins, J. 2018, TESS Science Data Products Description Document, Technical Report, https://ntrs.nasa.gov/archive/nasa/casi.ntrs.nasa.gov/20180007935.pdf
Thorngren, D. P., & Fortney, J. J. 2018, AJ, 155, 214
Thorngren, D. P., Fortney, J. J., Lopez, E. D., Berger, T. A., & Huber, D. 2021, ApJL, 909, L16
Tinetti, G., Drossart, P., Eccleston, P., et al. 2018, ExA, 46, 135
Tokovinin, A. 2020, MNRAS, 496, 987
Triaud, A. H. M. J. 2018, The Rossiter-McLaughlin Effect in Exoplanet Research (Berlin: Springer), 2
Tuomi, M., Jones, H. R. A., Barnes, J. R., Anglada-Escudé, G., & Jenkins, J. S. 2014, MNRAS, 441, 1545
Tuomi, M., Jones, H. R. A., Butler, R. P., et al. 2019, arXiv:1906.04644
Turrini, D., Schisano, E., Fonte, S., et al. 2021, ApJ, 909, 40
Van Cleve, J. E., Christiansen, J. L., Jenkins, J. M., et al. 2016, Kepler Data Characteristics Handbook, Kepler Science Document KSCI-19040-005
van der Walt, S., Colbert, S. C., & Varoquaux, G. 2011, CSE, 13, 22
van Roestel, J., Bellm, E. C., Duev, D. A., et al. 2019, RNAAS, 3, 136
Virtanen, P., Gommers, R., Oliphant, T. E., et al. 2020, NatMe, 17, 261
Wang, J., Fischer, D. A., Xie, J.-W., & Ciardi, D. R. 2014, ApJ, 791, 111
Wang, X.-Y., Rice, M., Wang, S., et al. 2022, ApJL, 926, L8
Wang, X.-Y., Wang, Y.-H., Wang, S., et al. 2021, ApJS, 255, 15
Weidenschilling, S. J., & Marzari, F. 1996, Natur, 384, 619
Welbanks, L., Madhusudhan, N., Allard, N. F., et al. 2019, ApJL, 887, L20
Wittenmyer, R. A., Wang, S., Horner, J., et al. 2020, MNRAS, 492, 377
Wright, E. L., Eisenhardt, P. R. M., Mainzer, A. K., et al. 2010, AJ, 140, 1868
Wright, J. T., Marcy, G. W., Howard, A. W., et al. 2012, ApJ, 753, 160
Wu, Y., & Murray, N. 2003, ApJ, 589, 605
Wu, D.-H., Rice, M., & Wang, S. 2023, AJ, 165, 171
Xiang, M. S., Liu, X. W., Yuan, H. B., et al. 2017, MNRAS, 467, 1890
Yan, R., Chen, Y., Lazarz, D., et al. 2019, ApJ, 883, 175
Yao, Y., Miller, A. A., Kulkarni, S. R., et al. 2019, ApJ, 886, 152
Yee, S. W., Petigura, E. A., & von Braun, K. 2017, ApJ, 836, 77
Youngblood, A., France, K., Loyd, R. O. P., et al. 2016, ApJ, 824, 101
Yuan, H. B., Liu, X. W., Huo, Z. Y., et al. 2015, MNRAS, 448, 855
Zechmeister, M., & Kürster, M. 2009, A&A, 496, 577
Zechmeister, M., Reiners, A., Amado, P. J., et al. 2018, A&A, 609, A12
Zhong, J., Lépine, S., Hou, J., et al. 2015, AJ, 150, 42
Zhong, J., Li, J., Carlin, J. L., et al. 2019, ApJS, 244, 8
Zhou, G., Huang, C. X., Bakos, G. Á, et al. 2019, AJ, 158, 141
Zhu, W. 2022, AJ, 164, 5
Zhu, W., Dai, F., & Masuda, K. 2018, RNAAS, 2, 160
Zhu, W., & Dong, S. 2021, ARA&A, 59, 291
Ziegler, C., Law, N. M., Baranec, C., et al. 2018, AJ, 156, 83
Ziegler, C., Tokovinin, A., Latiolais, M., et al. 2021, AJ, 162, 192